ADDIS ABABA UNIVERSITY

ADDIS ABABA INSTITUTE OF TECHNOLOGY

SCHOOL OF MULTIDISCIPLINARY ENGINEERING

CENTER FOR MATERIALS ENGINEERING

MASTER THESIS

First principles investigation of van der Waals heterostructures of MoS_2 and Janus transition metal dichalcogenides for energy applications.

A Thesis Submitted to Center for Materials Engineering in Partial Fulfillment of the Requirements for the Degree of Master of Science in Materials Engineering

BY:

Birhan Tesfaye Beshir

September 2021

Addis Ababa

Ethiopia

ADDIS ABABA UNIVERSITY

ADDIS ABABA INSTITUTE OF TECHNOLOGY

SCHOOL OF MULTIDISCIPLINARY ENGINEERING

CENTER FOR MATERIALS ENGINEERING

MASTER THESIS

First principles investigation of van der Waals heterostructures of MoS_2 and Janus transition metal dichalcogenides for energy applications.

BY: Birhan Tesfaye Beshir

A Thesis Submitted to Center for Materials Engineering in Partial Fulfillment of the Requirements for the Degree of Master of Science in Materials Engineering

Approved by Board of Examiners

Georgies Alene (Dr)	_____	_____
Advisor	Signature	Date
Tekalign Debela (Dr)	_____	_____
Co. Advisor	Signature	Date
Yedilfana Setarge (Dr)	_____	_____
External Examiner	Signature	Date
Sintayehu Nibret (Dr)	_____	_____
Internal Examiner	Signature	Date

DECLARATION

I hereby declare that the work which is being presented in this thesis entitled "First principles investigation of van der Waals heterostructures of MoS_2 and Janus transition metal dichalcogenides for energy applications." is new work of my own, has not been presented for a degree of any other university and all the resource materials used for this thesis have been accordingly acknowledged.

Name: Birhan Tesfaye Beshir

Signature: _____

Date of submission: ----------

ABSTRACT

Recent research on the Janus transition metal dichalcogenide (JTMD) with an asymmetric structure has revealed that this material possesses interesting unique properties, notably in solar cells. This work is based on cutting-edge density functional theory (DFT) computations utilizing Generalized Gradient Approximation- Perdew–Burke–Ernzerhof functional (GGA-PBE) as implemented in the Quantum ESPRESSO and VASP codes. To find the most stable optimized heterostructures, eight basic stacking patterns were designed. Then, for $MoSSe/MoS_2$, $WSSe/MoS_2$, and $MoSTe/MoS_2$ heterobilayer, the AAII-S stacking mode was more stable than the other stacking types. According to the findings, the band alignment was type-I for $MoSSe/MoS_2$, $MoSTe/MoS_2$, and type-II for $WSSe/MoS_2$, within, 1.03, 0.30 and 0.84 eV are estimated bandgap, respectively. The electrical band structure, as well as band edge placements, was investigated. When the water redox and oxidation potentials of heterostructures were compared, it was discovered that $MoSSe/MoS_2$, $MoSTe/MoS_2$, and $WSSe/MoS_2$ were not applicable for photocatalytic materials for full water splitting. On the other hand, $MoSSe/MoS_2$ and $MoSTe/MoS_2$ heterostructures were placed lower than the oxidation potential of O_2/H_2O, making them applicable for oxygen evolution reaction (OER). This work reveals that $JTMDs/MoS_2$ heterostructures are often subsequent material that promotes the development of photovoltaic devices, specially $MoSSe/MoS_2$, and $WSSe/MoS_2$ vdWH. The power conversion efficiency (PCE) of the heterostructures is calculated, and the results show that $MoSSe/MoS_2$ and $WSSe/MoS_2$ show very good efficiency with values of 19.41% and 16.25%, respectively. The result is good when compared to other similar studies: GaTe-InSe (9.1%), MoS_2/p-Si (5.23%), organic solar cells (11.7%), and PN-WSe_2 (13.8 %). Since the results are encouraging, we believe it is a good idea to do additional experiments on the heterostructures and adapt them to solar cell applications.

Keywords: $JTMDs/MoS_2$ heterostructures, DFT, bandgap, band alignment, photovoltaics, power conversion efficiency, photocatalyst, water splitting.

ACKNOWLEDGMENTS

Primarily, I would thank God for being able to complete this thesis and master's degree as well. Then I wish to express my sincere gratitude to my advisor Dr. Georgies Alene for his encouragement, continuous support, and guidance throughout the work of my MSc thesis.

Equivalently, I would like to thank Dr. Tekalign Debela (Research Professor, Jeonju University, Republic of Korea) for providing the necessary resources and continuous support without which, it would not have been possible to complete this thesis.

Finally, I would like to thank my family and friends who helped me a lot in finalizing this thesis. You are always there, not only for this work but all the time.

Contents

LIST OF TABLES

LIST OF FIGURES

LIST OF ACRONYMS

TMD	Transitional metal dichalcogenide
JTMDs	Janus transitional metal dichalcogenide
2D	Two-dimensional
DFT	Density-functional theory
DOS	Density of State
PDOS	Partial density of state
TDOS	Total density of state
GaAs	Gallium Arsenate
PP	Pseudopotential
Ry	Rydberg
eV	Electron Volt
E_b	Binding energy
LDA	Local-density approximation
GGA	Generalized Gradient Approximation
MoS_2	Molybdenum Disulfide
QE	Quantum ESPRESSO
PV	Photovoltaic
LED	Light-emitting diodes
hBN	hexagonal boron nitride
vdWH	Van der Waals heterostructure
PCE	power conversion efficiency
NHE	Normal hydrogen electrode

XC	Exchange-Correlation
VBM	Valence band maximum
CBM	Conduction band minimum
PBE	Perdew–Burke–Ernzerhof functional
HSE06	Heyd-Scuseria-Ernzerhof
SOC	Spin−Orbit Coupling
IR	Infrared
NIR,	Near-infrared
MIR	Mid-infrared
FIR	Far-infrared

CHAPTER ONE: INTRODUCTION

1.1 BACKGROUND OF THE STUDY

In recent years, the rapid expansion of modern industry and the global population have accelerated the consumption of energy. In 2015, worldwide primary energy consumption was ~$5.7*10^{20}$ J, which was equivalent to an average power use of 18.1 terawatts (TW)[1]. It is estimated that more than 80% of energy [2] (fig 1. a) is obtained from fossil fuels such as petroleum, oil, and natural gas, but there is a global motivation for the exploitation of sustainable and green energy to replace fossil fuels.

Renewable energy, such as solar, hydrogen, wind power, hydropower, biomass, biofuel, and geothermal energy, has been used to replace conventional fossil fuels due to its sustainability, low pollution, and inexhaustibility[1]. Compared to other clean and renewable energy sources, solar energy is by far the most promising energy source because they have the advantages of eco-friendly nature, zero-emission, and abundance. The amount of solar energy radiated on the surface of planet earth in one hour ($4.3 *10^{20}$ J) is comparable to all of the energy currently consumed on the planet in a year [1]. Unlike conventional power plants using coal, nuclear, oil, and gas, solar PV has no fuel costs and comparatively low operation, and maintenance costs [2]. Solar PV energy is primarily dependent on Si-based homojunction solar cells [3]. But, their efficiency is limited by the spectral, optical, and electrical losses [4]. Semiconductors with high mobility and direct bandgap near 1.3 eV are desired for high-efficiency single-junction PVs [5].

More recently, two-dimensional (2D) layered transition metal dichalcogenides (TMDs) with unique structural, physical, and chemical properties have attracted dramatically increasing interest for PVs, due to their potential in nanoelectronics, valleytronics, optoelectronics, and catalysis [6]. A recent investigation of JTMD has broad application prospects in PV cells. It is quite different from the properties of traditional 2D materials [7]. Like solar energy, much attention has been focused on energy shortages; one alternative that has attracted significant interest is hydrogen (H_2). At present, hydrogen is mainly produced from fossil fuels like natural gas by steam reforming[2]. In this technique, fossil fuels are consumed and CO_2 is emitted. Hydrogen needs to be produced from water using natural energies like sunlight if

one thinks of energy and environmental issues. There are several ways for solar hydrogen production, like (i) Electrolysis of water using a solar cell, hydroelectric power generation, (ii) Reforming of biomass. (iii) Photocatalytic or Photoelectrochemical water splitting. (Figure 1b) shows a possible pathway of hydrogen gas from production to final consumption. The recently emerged 2D layered materials have exhibited great potential for photocatalytic applications due to the large surface-volume ratio, numerous catalytic reactive sites, and therefore the ability of excellent optical adsorption[3].

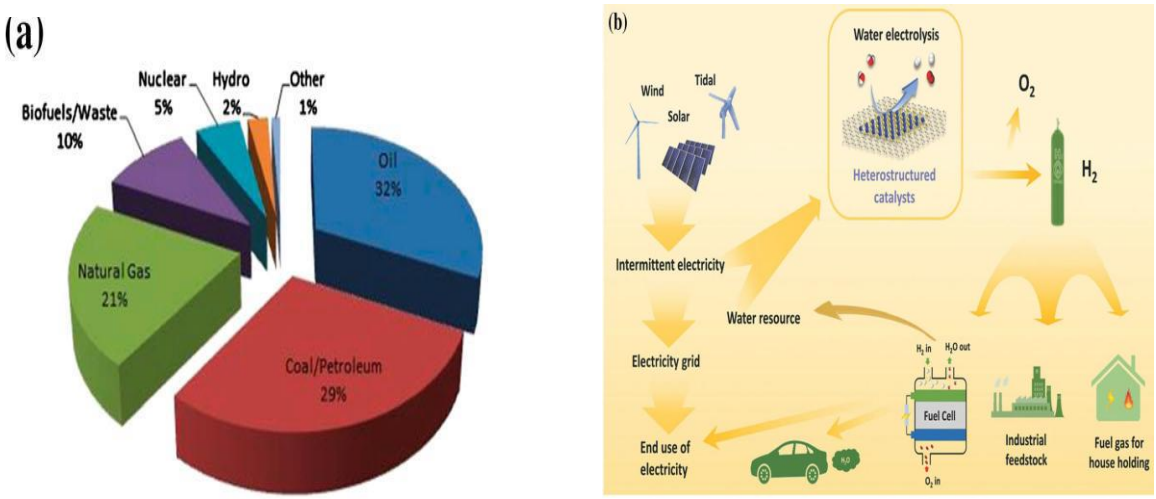

Figure 1 (a) The world's fuel shares[2]. (b) The pathway of hydrogen gas from production to utilization [2].

Coupled by weak van der Waals layer interactions, each TMDs layer with a regular formula MX_2 (M=Mo, W, and X=S, Se, Te) consists of a transition metal atomic layer sandwiched between two chalcogen atomic layers. The unique layered structure makes that few-layer and mono-layer JTMDs are thermodynamic stables [1]. The tunable electronic structures which strongly depend on the layer thickness and external stimuli facilitate the optical adsorption and thus the optimal band alignments. With the discovery of the first 2D material, graphene (honeycomb-patterned carbon monolayer), in 2004, interest in similar materials has grown rapidly as shown in Figure 2[4]. To realize the highly efficient optoelectronic devices based on the TMD monolayers, it is also important to develop a strategy to tune the band gaps of the TMD monolayers[5]. Amazingly, it has been reported that the 2D TMD materials can absorb up to 5 to 10% of incident sunlight in a thickness of

less than 1 nm and have been shown to achieve one order of magnitude higher sunlight absorption than the most commonly used solar absorbers such as GaAs and Si[6].

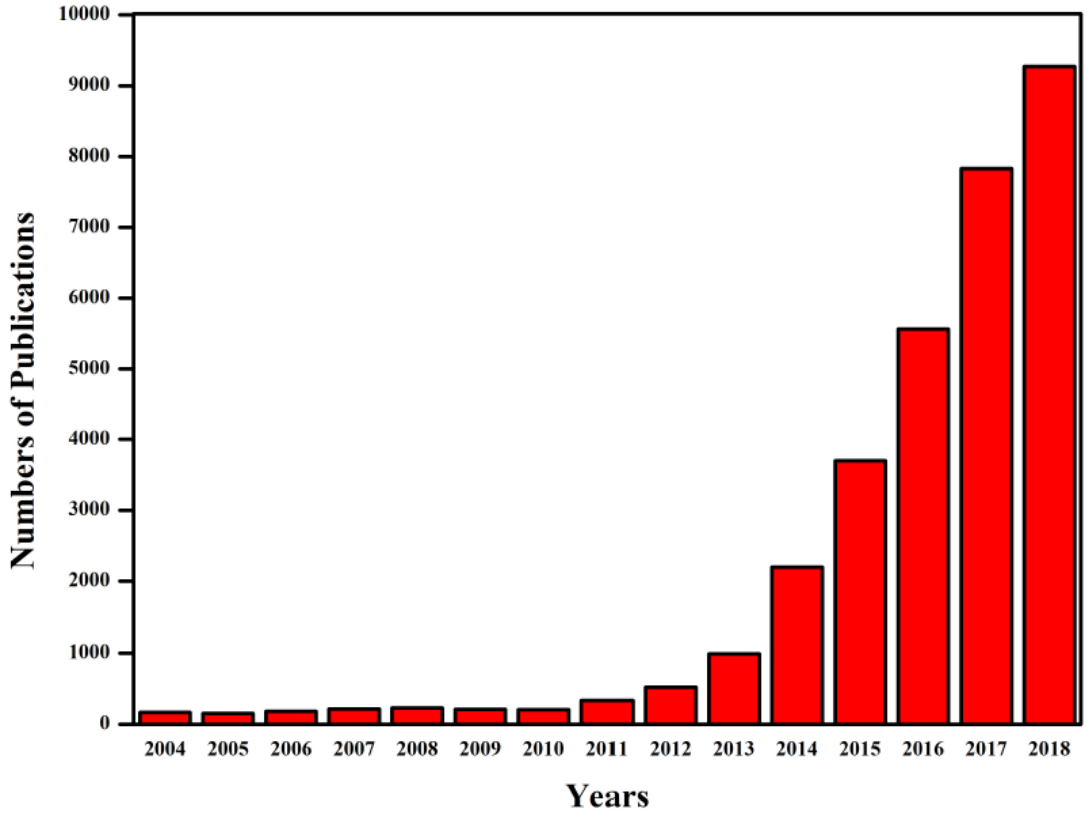

Figure 2 Number of published papers about "TMDs" by years[11]

Among TMDs, MoS_2 is the most interesting for its acceptable electrical, optoelectronic, and photocatalytic properties in a 2D state. In bulk, MoS_2 has a 1.29 eV bandgap with an indirect one yet shifted into 1.8-1.9 eV with a direct bandgap in 2D single layers. This value of the bandgap allows MoS_2 to be applied in semiconductor-based devices, including any energy devices. Several studies show MoS_2 application in solar cell, field effect transistor, and photoluminescence devices [12].

In this work focused on the basic properties of JTMDs /MoS_2 heterostructures. Janus 2D materials have attracted intensive research interest due to the unique properties induced by symmetry breaking, and promising applications in energy conversion. Motivated by the intriguing properties and multifunctional applications of 2D JTMDs, no previous study has investigated the vdWHs of MoS_2 and JTMDs for energy applications. This work, focused on energy applications through DFT, with PBE calculations as implemented in QE.

1.2 STATEMENT OF THE PROBLEM

Energy and environmental issues at a global level are important areas. It is essential to construct clean energy systems in order to solve the issues. Hydrogen and Solar energy are very important and promising clean energy, which has attracted much attention among various forms of renewable energy, to replace those nonrenewable energies, mainly because it has the advantages of eco-friendly nature, abundance, and zero-emission. Janus 2D materials have attracted intensive research interest due to the unique properties induced by symmetry breaking, and promising applications in energy conversion. Stacking different materials together can have numerous effects on the electronic, and photocatalytic properties of individual layers and thus the vdWH as an entire. However efficient PVs and photocatalyst materials are the main problems in the range of visible light irradiation. The bandgap of a visible-light-driven PV performance, promising photocatalyst, therefore, suitable band engineering is necessary for the design of photocatalyst, and PV with a visible light response. The heterostructures of JTMDs with MoS_2 Monolayer for PV devices, and photocatalyst, will have the potential to generate better efficiency.

1.3 OBJECTIVES

1.3.1 GENERAL OBJECTIVE

The general objective of this work is investigation of van der Waals heterostructures of MoS_2 and JTMDs for energy applications. A DFT study

1.3.2 SPECIFIC OBJECTIVES

The specific objectives of this research are:

- To determine the electronic properties, and PDOS of JTMDs/MoS_2 heterostructures.
- To get the most stable optimized JTMDs/MoS_2 heterostructures by applying different stacking patterns.
- To calculate band edge positions of JTMDs/MoS_2 heterostructures for photocatalyst material for water splitting.
- To calculate the power conversion efficiency and band alignment of JTMDs/MoS_2 heterostructures.

1.4 SCOPE AND LIMITATIONS OF THE STUDY

The study covers the investigation of the electronic, enhanced photovoltaic and photocatalytic performance of JTMDs/MoS_2 heterostructures using DFT. The scope of this study is only on the theoretical properties based on DFT without any experimental work. GGA-PBE approximation was only used and this approach underestimates the electronic properties of the structures. Other approaches that give better electronic properties such as HSE06 were not employed due to a lack of supercomputers.

1.5 SIGNIFICANCE OF THE STUDY

This computational work can be used as opening the base for future research studies related to the heterostructures of JTMDs with TMDs monolayer for PV devices, and photocatalyst materials. The output of the study can be used for solar cell manufacturing and hydrogen production industries. Additionally, it is better to bring experimental works and theoretical modeling features together to understand and study their photocatalytic efficiency, and electronic applications.

1.6 ORGANIZATION OF THE STUDY

The study is organized with in five chapters. Chapter one is introduction part which discusses background of the study, problem statement, objectives of the study, its significance and the scope. Literature reviews chapter two and chapter three research methodologies. Chapter four discusses and explanations of the study. Chapter five concludes the results of the study and recommends for action and further future research directions.

CHAPTER TWO: REVIEW OF RELATED LITERATURE

2 LITERATURE REVIEW

What would the properties of materials be if we could really arrange the atoms the way we might identify them? Asked Richard P. Feynman in 1959 during his well-known lecture entitled "There is plenty of room at the bottom"[14]. The idea of designing materials at the atomic level is very appealing, but almost 60 years after Feynman's talk, its implementation remains a major goal of materials science. One of the most successful approaches to date arose in the 70s with the development of multilayer (III-V) heterostructures grown by molecular beam epitaxy [15]. This key technology has led to many important optoelectronic applications, including semiconductor lasers, solar cells, and high-speed photodetectors, which have transformed our daily lives. Yet, various material constraints (e.g. lattice matching conditions) severely limit the standard and sort of these heterostructures [15], which involves a replacement material design strategy.

2.1 TWO-DIMENSIONAL (2D) MATERIALS AND THEIR HETEROSTRUCTURES

2D layered materials have recently emerged as a promising platform for the creation of a new type of heterostructure that overcomes the limitations of conventional materials. The heterojunction is that the interface that occurs between two layers or regions of dissimilar crystalline semiconductors. Heterostructure can be defined as the combination of multiple heterojunctions together during a device formation. The first isolation of graphene in 2004[15] and of other 2D crystals in 2005 [16] by Geim and Novoselov triggered enormous interest in these materials [16]. In their bulk form, these materials are formed by atoms with strong in-plane covalent bonds, while each layer is weakly bound to neighboring layers by van der Waals interactions. This weak interlayer interaction makes it possible to mechanically exfoliate individual layers from the bulk. Driven by the simplicity of this isolation method (the so-called "scotch-tape method"), a large research effort ensued that revealed the truly fascinating properties of graphene, including its high electronic mobility, large tensile strength, and superior thermal conductivity [17]. These crystals display a wide range of properties that complement those of gapless graphene. For example, hBN is a transparent insulator [18], while transition metal dichalcogenides [19], like MoS_2, are semiconductors with bandgaps in the near-infrared to the visible region (Fig.3). Moreover,

due to important changes in their electronic band structure, 2D materials typically display properties that are very different from those of their bulk counterparts. TMDs, for example, exhibit a crossover from indirect to direct bandgap in the monolayer limit [20].

2.1.1 OPTOELECTRONIC PROSPECTS

In recent years, the potential of 2D materials and their heterostructures for photonic and optoelectronic applications has become increasingly evident. A wide range of optoelectronic devices based on 2D materials have indeed been successfully demonstrated, including optical modulators, light-emitting diodes (LEDs), and plasmonic devices. Among these, photodetectors have undoubtedly attracted the most attention[7].

This 2D materials and their heterostructures for photonic and optoelectronic applications has been prompted by the prospects of photodetectors with superior performance in terms of efficiency, detection speed, as well as wavelength range, and mechanical flexibility. Indeed, 2D materials, especially graphene and TMDs, are appealing for photodetection applications[8]. Due to its gapless nature, graphene has broadband (Figure 3) and ultrafast photoresponse dominated by hot carriers, making it promising for high-speed photodetection.

In contrast, the optical response of semiconducting TMDs exhibits strong light-exciton interactions, valuable for applications demanding high light absorption. Combining these balancing properties during a single heterostructure is a promising approach for creating multi-functional, high-performance optoelectronic materials[9].

Therefore 2D materials have emerged as promising candidates in the field of material science, engineering, and nanotechnology. Layered 2D TMDs, most notably; MoS_2 and WS_2 have attracted significant attention due to their tunable and direct bandgap-dependent characteristics.

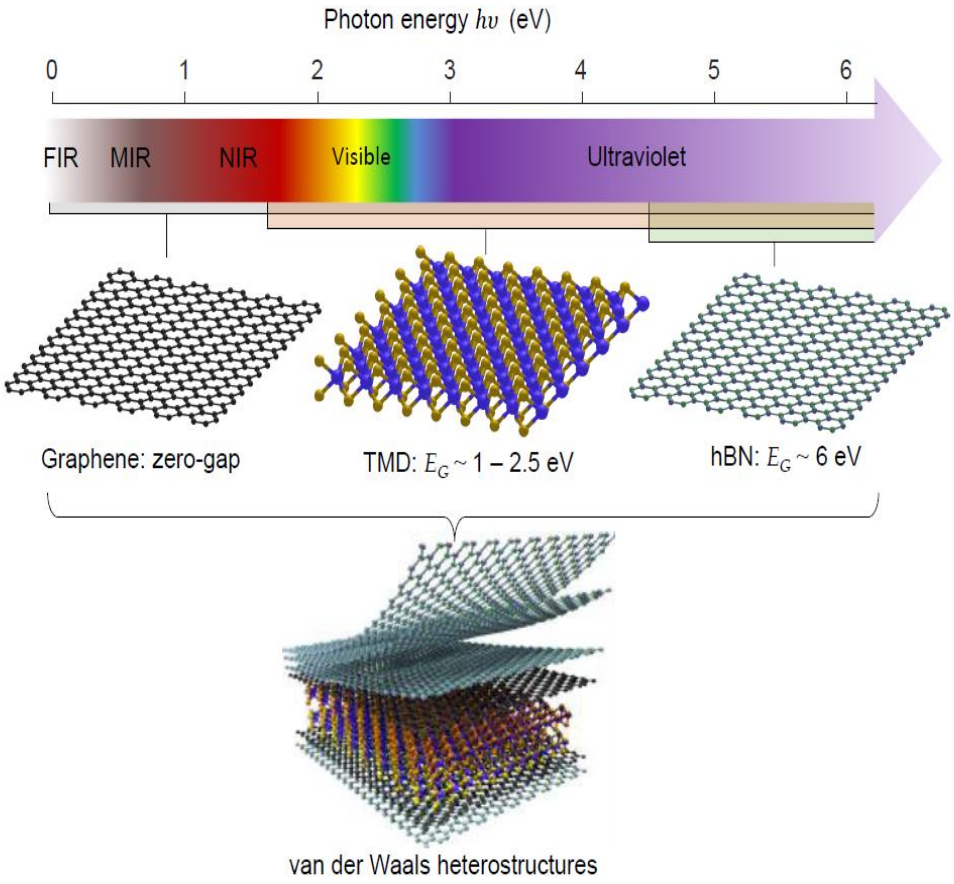

Figure 3 Overview of the optoelectronic properties of 2D materials and their heterostructures.

A schematic of vdWHs is shown in the lower portion of the panel [22].

2.2 TRANSITION METAL DICHALCOGENIDES

As we discussed in the previous section, the linear dispersion relation of graphene leads to unique optical and electrical properties, but the lack of a bandgap limits its use for many applications where semiconductors are needed. The search for other 2D materials with a bandgap has led to the discovery of monolayer (group-VI) transition metal dichalcogenides (TMDs), which most notably includes MoS_2, WS_2, $MoSe_2$, and WSe_2. Although TMDs in their layered bulk form have been studied for many decades[10][11], the properties of their mono- and few layers have only been investigated in recent years [12] [13] 14].

In the monolayer limit, TMDs possess a direct bandgap in the visible to the near-infrared region [15], as shown in figure 3, which makes them suitable for various electrical and optoelectronic applications. Combined with their relatively high mobility (1 - 100 cm^2 /Vs at

room temperature) [16], their sizable bandgap makes them attractive as a channel material in logic transistors[17]. TMDs have also aroused great interest due to their unique optical properties[18].

2.2.1 ELECTRONIC PROPERTIES OF TRANSITION METAL DICHALCOGENIDES

Coupled by weak van der Waals layer interactions, each TMDs layer with a regular formula MX_2 (M=Mo, W, and X=S, Se, Te) consists of a transition metal atomic layer sandwiched between two chalcogen atomic layers. Each monolayer consists of two planes of chalcogen atoms sandwiching a plane of metal atoms in the trigonal prismatic structure [22][19]. Monolayer TMDs have hexagonal out-of-plane symmetry, but unlike graphene, their in-plane inversion symmetry is broken. The electronic band structure of a solid describes the range of energies that the electrons within the solid can possess.

Due to quantum mechanical wave functions, the electrons within the solid can only possess a particular range of energy in certain locations within the band structure. The sameness of the periodic lattice, which is described by the Brillouin zone, allows using the band structure of a lattice to represent the band structure of the entire solid. The band theory has been utilized to elucidate many important physical properties and is essential in designing electronic and optoelectronic devices. Brillouin zone is usually utilized in mathematics and physics to explain the primitive cell in reciprocal space. The answer to the Bloch wave during a periodic medium is usually represented by their behavior during one Brillouin zone.

2.3 VAN DER WAALS HETEROSTRUCTURES

2D layered materials, like graphene, TMDs, and hBN, display good complementary properties. Interestingly, the same weak van der Waals forces that allow exfoliation of these bulk materials into single layers free of dangling bonds can also be used to stack them onto one another in the desired layer order. The resulting van der Waals heterostructures (vdWHs) combine the individual properties of the layers that they comprise and present new physical effects and interesting possibilities for engineering their optoelectronic properties. Indeed, the lack of lattice matching constraints introduces several degrees of freedom in the fabrication of these heterostructures, such as the thickness of the layers, their sequence, and their rotational alignment. Hence, with so many 2D materials to choose from, it is possible to create a large variety of vdWHs [20] [21] [22].

2D layered materials are atomically thin crystals where atoms are bond in a plane by fully saturated covalent bonds. Due to this particular atomic structure, 2D materials are in principle free of dangling bonds and surface trap states, and they interact with their neighboring layers via vdW forces. Since these forces are relatively weak compared to direct chemical bonds, layers with different atomic structures and rotational orientation can be vertically assembled without compromising the integrity of each layer or degrading their properties. Within vdWHs the lattice matching condition is drastically relaxed, allowing for the combination of any 2D layers, even with a large lattice mismatch[23].

Depending on the bandgaps, and the electronic affinity of semiconductors, heterostructures can be divided into three different cases: type-I, type-II, and type-III band alignment [36] as shown in Fig. 4. When material one and material two merge, the resulting heterostructure is Type-I if VBM1<VBM2<CBM2<CBM1, Type-II, if VBM1<VBM2<CBM1<CBM2 Type-III if VBM1<CBM1<VBM2<CBM2[24][25].

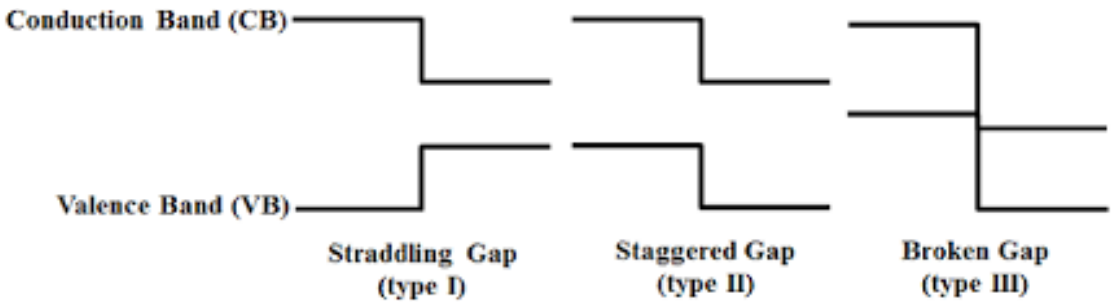

Figure 4 Energy band diagrams for Type-I, Type-II, and Type-III, heterojunctions [36].

Stacking different materials together can have numerous effects on the electronic properties of individual layers and therefore the vdWH as a whole[26]. These effects mostly depend on the electronic band alignment between the layers and on the strength of the interlayer coupling, which is in part determined by the rotational alignment and lattice mismatch of the layers. If the interlayer coupling is weak (which is normally the case for misoriented layers), individual layers largely preserve their 2D properties and interact with their neighboring layers via electrostatic coupling[27]. In this case, the electronic behavior of the vdWH is determined by the contribution of the individual layers and by the heterojunctions that they form.

2.4 STRUCTURE AND PROPERTIES OF MoS_2

Among TMDs, MoS_2 (Molybdenum Disulfide) is the most interesting for its fine electrical and optoelectronic properties in a 2D state. In bulk, MoS_2 to have 1.29 eV bandgap with indirect one yet shifted into 1.8-1.9 eV[28] with a direct bandgap in two-dimensional single layer[11]. In our PBE calculations, the MoS_2 monolayer as shown in figure 5 is a direct bandgap with a bandgap of 1.74 eV. This value of the bandgap allows MoS_2 to be applied in semiconductor-based devices, including any energy devices. Several studies show MoS_2 application in solar cell, FET, and photoluminescence devices[29].

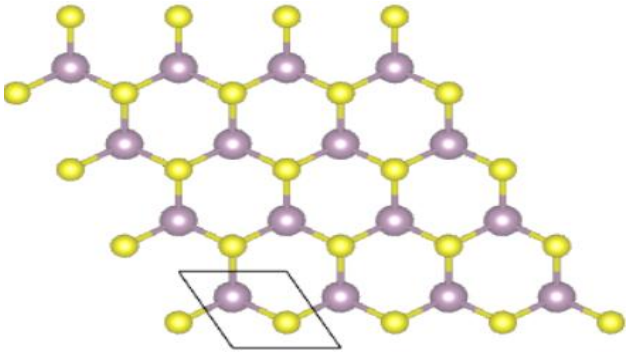

Figure 5 The single-layer MoS_2 structure: Brown: molybdenum, yellow: sulfur atoms

2.5 JTMDs MONOLAYERS PVs, and PHOTOCATALYST MATERIALS FOR WATER SPLITTING

Due to the continuous growth of energy crises and environmental pollutions, photocatalysis, as a promising technology[30] to simultaneously solve these two problems by utilizing solar energy, has attracted significant interest in recent years[31]. Using the photo-generated electrons and holes of photocatalysts, H_2O can be split into value-added chemical fuels, hydrogen, which is a “green” route to convert solar energy into chemical energy without environmental pollutions. The recently emerged 2D layered materials have exhibited great potential for photocatalytic applications due to the large surface-volume ratio, numerous catalytic reactive sites, and therefore the ability of excellent optical adsorption[32]. The tunable electronic structures which strongly depend rely on the layer thickness and external stimuli facilitate the optical adsorption and therefore the optimal band alignments relative to the redox potential of water. Consequently, 2D materials usually have better photocatalytic performances than their bulk counterparts.

However, the achieved photocatalytic efficiency of 2D materials so far isn't as high as expected due to some practical reasons. Typically, a perfect photocatalyst has got to be stable under atmosphere environments and semiconducting with medium band gaps as an insulator. Structural symmetry-breaking plays an important character within determination of the electronic band structures of two-dimensional materials. Most studies argued that the JTMDs van der Waals heterostructures exhibit type-II band alignment, and propose that the JTMD monolayers are a promising candidate for electronics, PVs, and photocatalysis.

2.6 WATER ELECTROLYSIS

In response to the demand for hydrogen for use in the chemical and energy industries, water electrolysis has been a result since the early 20th century[33]. This technological conception uses electricity to resolve water motes in order to form oxygen and hydrogen gases in a device called an electrolyzer[34]. Decomposition of water occurs due to a direct current (DC) passed between two electrodes (cathode and anode) which are submerged in water separated by an ion-conducting (aqueous or solid) electrolyte. The total energy needed for electrolytic hydrogen product at standard temperature and pressure (293 K and 1 atm) is shown below in equation (2.1).

$$\Delta G° = \Delta H° - T\Delta S° = (286.03 - 0.163 \cdot T)\,\frac{KJ}{mol}\,H_2 \qquad (2.1)$$

The Gibb's free energy (ΔG°) corresponds to the minimum share of enthalpy (ΔH°) which has to be applied as work (electricity). The temperature and change in entropy (TΔS°) correspond to the maximum share of ΔH° which can be applied as thermal energy to the process. The overall electrolysis reaction (shown below) is a sum of two electrochemical reactions (also called the half reactions or the half-cell reactions), which occur at the electrodes[35]. The stoichiometric net energetic reaction of electrolysis of water is described in equation (2.2)

$$H_2(l) + 237.2\,\frac{KJ}{mol} + 48.7\,\frac{KJ}{mol} \rightleftarrows\ H_2(g) + \frac{1}{2}O_2(g) \qquad (2.2)$$

The necessary energy to split water to generate oxygen and hydrogen gases is approximately 286 kJ/mol. This is derived from the enthalpy change for the combustion energy of hydrogen, also known as the higher heating value (HHV); approximately, + 237 kJ of this

energy derives directly from electrical energy, represented as the Gibbs free energy, the rest (48 kJ/mol) is derived from heat. the Gibbs free energy is rewritten below, which expresses the change in free energy for any extent of reaction:

$$\Delta G^{O} = -nFE^{O} \quad (2.3)$$

where n is the number of electrons transferred in the reaction, F is the Faraday constant (96,500 C/mol), and E^{O} is the change in potential (E^{O}= E^{O} reduction− E^{O} oxidation)[36]. This can be rewritten in terms of electrochemical equations and charges involved in the complete reaction (2.4) and two half- reactions: the oxygen evolution reaction (OER) and the hydrogen evolution reaction (HER), written below as it occurs in acidic conditions as (2.5) and (2.6) respectively:

$$2H_2O + 4h^+ + 4e^- \rightleftarrows 2H_2 + O_2 \quad (2.4)$$

$$2H_2O + 4h^+ \rightleftarrows O_2 + 4e^- + 4H^+ \qquad E^0 H_2O = 1.23\ V\ vs.\ NHE \quad (2.5)$$

$$4e^- + 4H^+ \rightleftarrows 2H_2 \qquad E^0 H^+/H_2 = 0.00\ V\ vs.\ NHE \quad (2.6)$$

Where E^0 is the energetic potential at standard temperature and pressure, STP, (25°C and 1bar) and the redox potentials for both the OER and HER are referenced to the normal hydrogen electrode (NHE).

2.7 BASICS OF PHOTOCATALYTIC WATER SPLITTING

Semiconductor devices have a band structure in which the conduction band is separated from the valence band by a bandgap with an appropriate width. When the energy of incident light is larger than that of a bandgap, electrons and holes are produced in the conduction and valence bands, respectively. The main processes in a photocatalytic reaction are, the first step is the absorption of photons to form electron–hole pairs, the second step is consists of charge separation and migration of photogenerated carriers, and the final step involves the surface chemical reactions as shown in figure 6 [2].(i) photon absorption. The absorption range of the solar spectrum depends on the energy band size of the semiconductor material, the smaller the bandgap, the wider the absorption range. The photogenerated hole initiates

the oxygen evolution reaction (OER; $2H_2O \rightarrow O_2 + 4e^- + 4H^+$; E = 1.23 V vs NHE). On the other hand, the electron initiates the hydrogen evolution reaction (HER; $2e^- + 2H^+ \rightarrow H_2$; E = 0.0 V vs NHE). The overall reaction-free energy change for the water-splitting process is 1.23 eV.

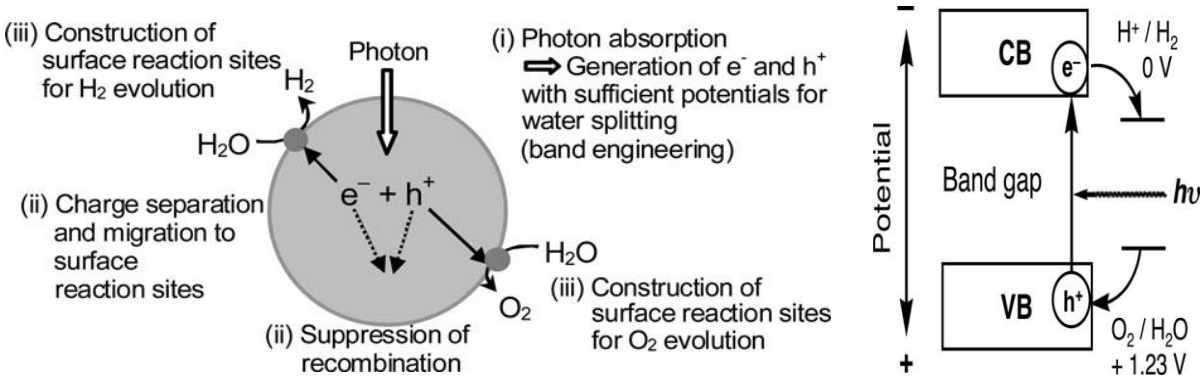

Figure 6 (a) processes in photocatalytic water splitting (b) Photocatalytic reactions[47]

(ii) photo-generated charge transfer. The crystal structure, crystallinity, particle size, and other factors of the material have an important influence on the separation and migration of photo-generated charges. Defects will become the trapping and recombination centers of photogenerated charges, so the better the crystallinity, and the fewer the defects and the higher the catalytic activity. The photo generated charge carriers migrate to the surface of the photocatalysts and then react with water under the suitable condition of valence and conduction band positions with respect to the water oxidation and reduction potentials. Consequently, a suitable bandgap and appropriate redox potential of the photocatalysts are prerequisites for an efficient photocatalytic water-splitting reaction.

(iii) Surface redox reaction. The surface reaction active sites and the specific surface area have an important influence on this process. Even if the photogenerated electrons and holes possess thermodynamically suitable potentials for water splitting, they will have to recombine with each other if the active sites for redox reactions do not exist on the surface[37].

2.8 THE OPTICAL ABSORPTION PROPERTIES OF JTMD MONOLAYERS

The optical absorption properties of JTMD monolayers are studied by computing the complex dielectric function $\varepsilon(\omega) = \varepsilon_1(\omega) + \varepsilon_2(\omega)$, where the imaginary part $\varepsilon_2(\omega)$ is related to

the absorption at a given frequency ω and the real part $\varepsilon_1(\omega)$ can be obtained from $\varepsilon_2(\omega)$ by the Kramers-Kronig relation. The absorption coefficient is evaluated by the following formula,

$$\alpha(\omega) = \frac{2\omega}{c\hbar}\left(\frac{\sqrt{\varepsilon_1^2 + \varepsilon_2^2} - \varepsilon_1}{2}\right)^{\frac{1}{2}}$$

where c represents the speed of light in a vacuum and ω is angular frequency.

Figure 7 shows the optical absorption spectrum of Janus monolayers as a function of photon energy. It may be created that the absorption spectrum α(ω) displays strong anisotropy along together with two polarization directions. Overall, the spectrum of α (ω) perpendicular has a clear blue shift as compared to that of parallel α (ω), resulting in a weak visible-light absorption along the out-of-plane direction. Consequently, as the optical absorber for solar cells and photocatalysts, the JTMD monolayers would be parallel to the light source thus as to obtain high absorption efficiency[38].

For the in-plane direction, the JTMD monolayers show strong absorption when the photon energy is beyond 2 eV (Figure 7 a). Remarkably, the absorption coefficient of MoSeTe, WSeTe, and WSTe can reach 3.5×10^5 cm^{-1} at the visible-light region[39], which is comparable to the conventional optical-absorber materials, such as CdTe, CIGS, and hybrid halide perovskites. Moreover, a prominent absorption peak located at 2.4~3.3 eV can be identified in six Janus systems, which arises from the d-d transitions[38][40].

The band-edge states of the Janus monolayers are primarily contributed by the d electrons of Mo or W atoms that have larger dispersion than s and p electrons. Thus, the d-d transitions are responsible for the high absorption efficiency of the Janus monolayers along the in-plane direction. Temporarily, the position of absorption edges and peaks in the Janus systems is different due to the difference in band structures. Obviously, the increase of bandgap leads to a blue shift of the absorption edges/peaks.

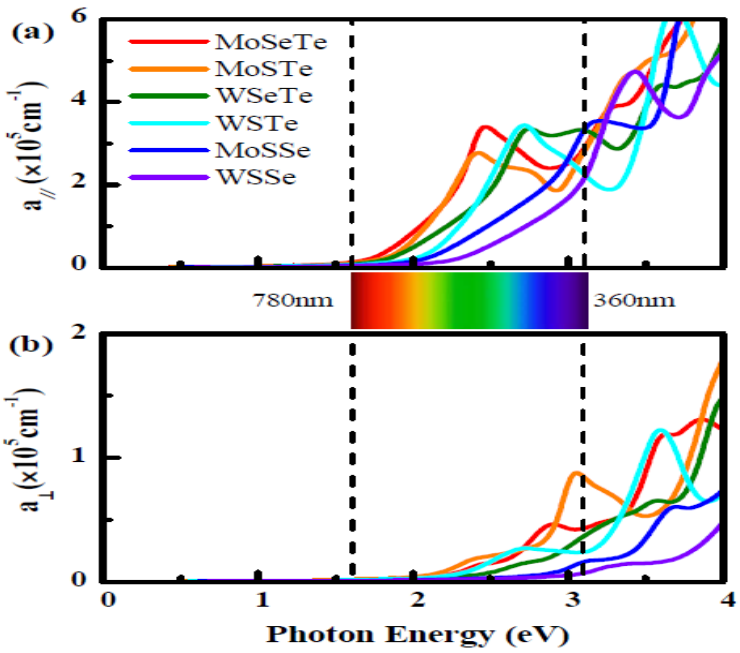

Figure 7 Optical absorption spectra of six JTMD monolayers out-of-plane (α⊥(ω)) directions calculated by the HSE, and SOC method. The dash lines denote the range of visible light from 360 to 780 nm[38] this is often why the narrower bandgap MoSeTe, WSeTe, and WSTe possess higher absorption efficiency in the visible-light range relative to other wide bandgap Janus systems.

2.9 THEORETICAL EFFICIENCY LIMIT OF SEMICONDUCTOR SOLAR CELLS

The maximum power conversion efficiency (PCE) of graphene-semiconductor solar cells is calculated. The performance of graphene-semiconductor solar cells as a function of the interface Schottky barrier height, and therefore, the bandgap of semiconductors is investigated [47]. Within ideal conditions, these photovoltaic cells reveal a bandgap range maximum[41] at Eg =1.1–1.7 eV with power conversion efficiency exceeding 25%. The efficiency of graphene/silicon and graphene/GaAs solar cells is 25.5% and 27.5%, respectively. The results of environmental temperature on the photovoltaic cell performance are additionally investigated, and it's found that to an honest degree, the facility conversion effectiveness of graphene-semiconductor solar cells varies linearly with temperature [47].

Table 1. Ideal performance metrics of graphene/silicon and graphene/GaAs solar cells under AM1.5 illumination at T=300 K[42]. The effective Richardson constants used in the ß=2

calculations are as follows: A*p_Si = 0.27A; An_Si = 0.93A, A*p_GaAs = 0.62A, A*n_GaAs =0.072A, where A is the Richardson constant of free electrons[42].

	silicon			GaAs		
ß (type)	1	2(p)	2(n)	1	2(p)	2(n)
Jsc ($mAcm^{-2}$)	43.64	43.64	43.64	31.50	31.50	31.50
V_{oc} (V)	0.69	0.65	0.62	0.98	0.93	0.99
FF	0.84	0.84	0.83	0.88	0.88	0.88
Efficiency(η%)	25.50	24.00	22.66	27.52	25.86	27.57

In this study, as shown in chapter 4, the band structure, PDOS, and band edge positions 2D JTMDs/MoS_2 heterostructures were calculated. The electronic band structure, band alignment, and band edge positions were calculated. vdW heterobilayer MoSSe/MoS_2, and MoSTe/MoS_2 type-I, and WSSe/MoS_2 type-II band alignment were designed. The electronic properties, the photovoltaic and photocatalytic performance of 2D JTMDs/MoS_2 heterostructures are studied using first-principles calculations based on DFT.

CHAPTER THREE: METHODOLOGY

3. COMPUTATIONAL METHOD

In this part, the application of the first principle calculation is to determine the band structure, electronic properties, band edge positions, and band alignment of new materials is explained. The microscopic description of the physical and chemical properties of a material system is a complex problem. In general, we have a collection of atoms interacting with forces that derive from some potential field. This ensemble of particles may be isolated (molecules and clusters), extended (solids, surfaces, wires, and liquids), or a combination of both (molecules in solution). However, altogether cases, we will unambiguously describe the system by a variety of nuclei and electrons interacting through Coulombic (electrostatic) forces. Electrons are fermions so that the total electronic wave function must be antisymmetric with respect to the exchange of two electrons. All the components are perfectly known and, in principle, all the properties can be derived by solving the Schrödinger equation. Electronic structure methods apply the laws of quantum mechanics to get properties of chemical species[43]. The foundation of these methods is to attempt to solve the Schrodinger equation:

$$H\Psi(r, t) = \frac{ih}{2\pi}\frac{\partial\Psi(r,t)}{\partial t} \tag{3.1}$$

where H is the Hamiltonian operator of the system, which is represented by the wave function, and which has a probability distribution $|\Psi^2|$ this is the probability that the system will be in a given state. If we consider that the systems potential energy (V), is time-independent, we get the time-independent Schrödinger equation:

$$H\Psi = E\Psi \tag{3.2}$$

Where, E is the Hamiltonian eigenvalue operator.

To do calculation of these eigenvalues, the systems Hamiltonian can be split up into different contributions, the Hamiltonian for this equation is:

$$H = T^{e}(r) + T^{n}(R) + V^{n\text{-}e} + V^{e}(r) + V^{n}(R) \tag{3.3}$$

where the superscripts n and e refer to the nucleus and electrons respectively, V is potential energy, T is kinetic energy and R and r refer to nuclear and electron position respectively.

In practice, the Schrödinger equation is almost impossible to treat in a full quantum mechanical framework. Only in rare cases, a complete analytic solution is available, and numerical solutions are also limited to a very small number of particles. There are several features that contribute to the present difficulty. First, this is often a many-body system, where each component (each nuclear species and therefore the electrons) obeys particular statistics. Additionally, the whole wave function cannot be easily factorized due to Coulombic correlations[44]. In other words, the complete Schrödinger equation can't be easily decoupled into a group of equations. The dynamics are an even more difficult problem, and very few and limited numerical techniques have been devised to solve it. Numeral approximations are necessary to solve the Schrodinger equation[45].

The first important approximation which is formed is that the Born-Oppenheimer (BO) approximation. The BO approximation is that as long as electrons are much lighter than the nucleus and thus move far more rapidly the motions of the nucleus and electrons are frequently decoupled, the electrons are assumed to be always equilibrated, and therefore, forces on the nuclei arise only as a result of atomic positions[46]. Thus the electronic structure part of the problem is reduced to that of solving the time-independent Schrodinger equation, with the electrons assumed to be in the ground state. This removes the second term from the above equation, yielding the electronic Hamiltonian, H^e.

3.1 DENSITY FUNCTIONAL THEORY (DFT)

The central focus of DFT is the electron density (ρ) and not the wave function as in Hartree-Fock methods. It is called a functional theory as the energy is a function of the density, E [ρ], which in turn is a function of the position, $\rho(r)$. A functional is a function of a function[47]. Though, DFT allows us to sidestep that computational difficulty by that specify in the electron density, rather than the many-body wave function. The central principle of DFT is that the entire energy of the system may be a unique function of the electron density, hence it's unnecessary to compute the complete Schrödinger equation of the system but, the specific functional dependence of the energy on the density is not known[48]. In these DFT formalisms the energy is split up as follows:

$$E_{DFT}[\rho] = T_s[\rho] + E_{ne}[\rho] + U[\rho] + E_{xc}[\rho] \quad (3.4)$$

With T_s [ρ] the electron kinetic energy, E_{ne} [ρ] the potential nuclear-electron interaction energy, and U [ρ] the potential electron-electron interaction energy, the final term E_{xc} [ρ] is the exchange-correlation energy which is calculated with an exchange-correlation functional. The choice of this last functional is where different DFT methods diverge and is vital to the success of the method. Kohn and Sham converted this DFT problem by calculating the ground state energy and particle density of an N-electron system to that of solving a set of independent-particle equations [48].

These Kohn–Sham equations contain N single-particle Schrödinger-like equations with a modified effective potential and are much easier to unravel than the many-body problems. No appearance for this exchange-correlation (E_{XC}) potential is known, but as it is relatively small compared with the fractional error arising from its approximation [48]. The Hohenberg-Kohn theorem demonstrates that there is a functional relationship between the electron density, ρ, and all observable properties of the interacting system of particles, meaning that all properties of the system may be determined if the electron density is known. We start by assuming that there exist two different potentials U and U′ which yield the same electron density, ρ, these two external potentials generate different operators V and V′ which in turn yield two different Hamiltonians H and H′. These systems also will have different wave functions Ψ and Ψ′ with energies E and E′ the energies are given by :

Proof

$$E = \langle \Psi \mid H \mid \Psi \rangle \quad (3.5)$$

$$E' = \langle \Psi' \mid H' \mid \Psi' \rangle$$

Now by applying the variational principle we can say that the exact Hamiltonian for a system always yields lower energy than an approximate one thus:

$$E' = \langle \Psi \mid H \mid \Psi \rangle < \langle \Psi \mid H' \mid \Psi \rangle \quad (3.6)$$

$$E = \langle \Psi' \mid H' \mid \Psi' \rangle < \langle \Psi' \mid H \mid \Psi' \rangle$$

We can also say that

$$\langle \Psi \mid H' \mid \Psi \rangle = \langle \Psi \mid H + V' - V \mid \Psi \rangle \quad (3.7)$$

$$\langle \Psi' \mid H \mid \Psi' \rangle = \langle \Psi \mid H' + V' - V \mid \Psi' \rangle$$

Assuming that

$$\langle \Psi' \mid \rho \mid \Psi' \rangle = \rho(r) = \langle \Psi' \mid \rho \mid \Psi' \rangle$$

(3.8)

Which is our original assumption, we obtain that

$$E' < \langle \Psi \mid H \mid \Psi \rangle + \int dr[u'(r) - u(r)]\rho(r) = E + \int dr[u'(r) - u(r)]\rho(r)$$

(3.9)

$$E < \langle \Psi' \mid H' \mid \Psi' \rangle + \int dr[u(r) - u'(r)]\rho(r) = E' + \int dr[u(r) - u'(r)]\rho(r)$$

(3.10)

Adding these two inequalities yields:

$$E' + E < E + E' \qquad (3.11)$$

This result is inconsistent and thus proves that the original assumption is false.

3.2 LOCAL DENSITY APPROXIMATION (LDA)

The functional is the Local Density Approximation, this approximation however tends to break down if the electron density is not close to homogenous. The LDA of a finite system with variable density ρ(r) consists of assuming the local EXC-density to be that of the corresponding infinite system with density ρ = ρ(r). In regions where the charge density is slowly varying, the exchange-correlation energy at that time is often considered an equivalent as that for a locally uniform electron gas of the same charge density. The LDA uniform works practically well in systems where the charge density is rapidly varying. In order to maneuver beyond the LDA, the addition of gradient corrections to include longer-range gradient effects is important[49].

$$E_{XC}^{LDA}[n] = \int (r)\, \varepsilon_{XC}^{unif}\, n(r)dr \qquad (3.12)$$

Where $\varepsilon_{xc}\ unif$ is the exchange-correlation energy per particle of the interacting uniform electron gas of density n(r).

3.3 GENERALIZED GRADIENT APPROXIMATION (GGA)

In addition to LDA approximation is the Generalized Gradient Approximation (GGA) which includes the first derivative (the gradient) of electron density when calculating Exc [ρ]. Furthermore, LDA includes a dependence on the local density gradient as in the generalized-gradient approximations (GGAs) with the PW91 and Perdew, Becke, and Ernzerhof (PBE) functionals. These extensions maintain the spherical average of the exchange-correlation hole, regularly supported the effect of weak perturbations on the homogeneous electron gas solids[50].

$$E_{XC}^{GGA}[n] = \int (r)\ \varepsilon_{XC}^{GGA}\ |\nabla n(r)|\ n(r)dr \tag{3.13}$$

Where, ∇n(r) is gradient of the density. Generalized-gradient approximations systematically improve the atomization energies of a good range of molecules and solids and proper the LDA's severe over-bindings. Once an E_{XC} potential has been chosen, what remains is the determination basis set for the single-particle wave functions[51].

3.4 THE PLANE WAVE PSEUDOPOTENTIAL METHOD

The plane wave pseudopotential method is one of the most widely used implementations the Kohn-Sham formulation of DFT. Plane Waves as a Basis When studying the electronic structure of condensed matter systems, one is investigating the behavior of a number of electrons in the order of 10^{28} per mole of atoms. Many extended systems are periodic in structure, corresponding to one of the Bravais lattices, so one can define an infinite periodic system and perform calculations for only the electrons in the periodic cell. Bloch's theorem shows that the wavefunction ψ, of an electron in bands n, for a periodic system can be expressed as a combination of a plane wave part and a periodic cell part[52]:

$$\psi_n\,(r) = u_n\,(r)^{\,ik.r} \tag{3.14}$$

Where,, the plane wave part has wave vector k, which is confined to the first Brillouin zone. The periodic part has the same periodicity as the lattice.

$$u_n\,(r + R) = u(r) \tag{3.15}$$

where R is one of the lattice vectors. This leads us to choose a plane wave basis set to describe the wavefunction within the periodic cell.

The periodic part of the wavefunction can then be written as:

$$u(r) = \sum_G C_{n,G} e^{iG.r} \quad (3.16)$$

Where we have plane wave coefficients C_n and G are the reciprocal lattice vectors that satisfy the relation $G = 2\pi m$ where m is an integer. If we combine equations 3.15 and 3.16, the Kohn-Sham orbitals can therefore be written as an infinite sum of plane waves:

$$\Psi n(r) = \sum_G C_{n,(K+G)} e^{i(G+G).r} \quad (3.17)$$

Where C_n, K+G are the coefficients of the plane waves describing the wavefunction.

Bloch's theorem allows us to require an infinite system but only calculate a finite number of electronic wavefunctions. However, this leaves an infinite number of k-points as each electron occupies a definite K[53]. In practice, we'd like only choose a sample of k-points because the wavefunction varies slowly over small regions of k-space. The electronic wavefunctions at k-points that are close are nearly identical. Therefore, a region of k-space is represented by the wave function at a single k-point. K-point sampling schemes are developed, like the one given by Monkhorst and Pack. The symmetry of the lattice is accustomed reduce the amount of k-points required.

The Brillouin zone are often made irreducible by applying the purpose group symmetries of the lattice, leaving no k-points related by symmetry. The sum over G vectors within the equation is infinite so as to completely describe the wavefunction, i.e. for the plane-wave basis set to be complete. When devising a computational implementation, one must choose a finite end to the sum. for many realistic wavefunctions, there'll be a scale below which the wavefunction will be described as smoothly varying. this implies that the coefficients C_n, k+G will become small for large K+G[54]. The cutoff point is said because the plane wave kinetic energy cutoff:

$$E_{cut} \geq \frac{1}{2} |K + G|^2 \quad (3.18)$$

i.e. it is greater than or equal to the highest kinetic energy of the plane waves used. This corresponds to a sphere in reciprocal space within which all the used |K+G| vectors lie.

When performing calculations one must always be careful to select an appropriate sampling of k-points and plane wave cutoff energy. This is done by performing calculations at successively higher cutoff energies and finer grids of k-points until the quantities of interest no longer change - a test of convergence.

3.5 KOHN-SHAM EQUATIONS

Practical DFT is nearly always done within the framework established by Kohn and Sham in 1965[44]. The first and second Hohenberg-Kohn theorem, define the playground for DFT. Everything that is constructed based upon these two theorems is a DFT. But within DFT there are several different ways of making practical calculations and the method of Kohn and Sham is a method so universally used that it is for practical purposes almost equivalent to DFT. What does the Kohn-Sham method tell us: No derivation is given just the final result? It gives us a practical way to find that ground-state density. The ground state density can be written as a sum of over-products between single-particle wave functions times their complex conjugate, and if this is for a system with N electrons there will be N such products. The Hamiltonian for that single-particle equation looks like, that Kohn-sham Hamiltonian; It has the kinetic energy, the Hartree energy of the particle which is the coulomb energy of that particle in the potential generated by all the other particles in the problem, the third term is the external potential: the Coulomb energy of the particle in the external potential, the fourth term is the exchange-correlation energy of the particle it is unique! Functional. If you know this one it is valid for all solid and molecules as soon as we have this unique exchange-correlation functional, the method of Kohn and sham gives us a unique and exact way to find the ground state density.

The exact ground state density of a N- electron system is

$$\rho(\vec{r}) = \sum_{i=1}^{N} \varphi_i^* (\vec{r})\, \varphi_i(\vec{r}) \qquad 3.19$$

Where, the single-particle wave functions φ_i are the N lowest-energy solutions of the Kohn-Sham equations.

$$H_{KS}\varphi_i = \varepsilon_i \varphi_i \qquad (3.20)$$

$$\text{With } H_{KS} = H + V_H + V_{ext} + V_{Exc} \qquad (3.21)$$

And $V_{Exc} = \delta V_{XC}(\rho)/\delta\rho$ (3.22)

The Kohn- Sham equations are an exact transformation of the original problem (coupled differential equations) in single-particle equations (uncoupled). The exchange-correlation potential is local in real space, so that it is usually calculated by evaluating the appropriate expression for the electronic density calculated on the real-space mesh associated with the PW expansion[54].

3.6 THE PSEUDOPOTENTIAL APPROXIMATION

Electrons in the neighborhood of the nuclei will be under the influence of steep Coulomb potential and have rapidly varying wave functions in the nuclear regions. This needs a correspondingly large number of plane waves to sufficiently to describe the wave function and the nuclear potential. In overall, there are two main purposes of pseudopotential formalism. First, to use a much weaker pseudopotential to get rid of core electrons which due to their deep potential would need to be described by many plane-wave basis functions. Second, to eliminate the rapid oscillations of the valence electron wavefunctions in the core region.

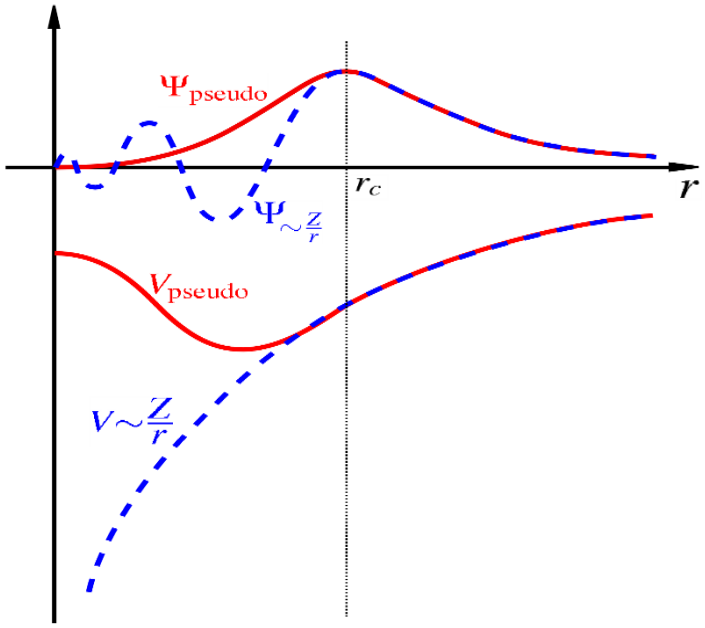

Schematic illustration of all-electron (dashed lines) and pseudopotential (solid lines) and their corresponding wave functions. The radius at which the all-electron and pseudo-electron values match is designated as r_c

3.7 SIMULATION SOFTWARE

The wide use of DFT simulations has only been made possible by the development of robust, high-performance density functional computer programs. For a materials simulation to possess predictive power, the simulation software itself must be robust enough to supply accurate results even when the modeled system is under extreme or unusual conditions, and fast enough to perform simulations with an inexpensive amount of computer time. In this work, we used DFT simulation software like Quantum-ESPRESSO, VASP, Materials Studio, and VESTA codes.

3.7.1 QUANTUM ESPRESSO

Quantum Espresso is an integrated software suite used for "ab initio" calculations to analyze the electronic structure simulation and materials modeling. This suite is free for the public under GNU general public license. QE includes independent and interoperable codes to serve the purpose[55]. The codes have been developed on the basis of DFT, Plane-wave expansion method, Pseudopotential Method. It uses different types of pseudopotentials such as coulomb potential, PAW, norm-conserving, and ultra-soft kinds. The plane wave density functional which is required to solve the KS equation is produced by running a plane wave self-consistent field (PWscf) program in presence of a suitable pseudopotentials file. Then the wave function is utilized for various electronic properties. Quantum Espresso has different distributions for different purposes[56].

3.8 SHORT-CIRCUIT CURRENT, OPEN-CIRCUIT VOLTAGE, AND MAXIMUM THEORETICAL EFFICIENCY.

For a light absorber with an optical bandgap (E_g), the maximum short-circuit current density (J_{SC}) can be estimated by assuming that all photons with energy larger than E_g are absorbed and always produce an electron−hole pair upon absorption:[58]

$$J_{SC} = e \int_{Eg}^{\infty} \frac{S(E)}{E} dE \tag{3.23}$$

where e is the electronic charge, S(E) the power radiated by the sun on earth per unit area and per unit of photon energy, and E the energy of an incident photon.

The open-circuit voltage can be expressed in terms of the bandgap of the light absorber and a variable parameter, called the loss-in-potential E_{loss}, as [59]

$$eV_{oc} = E_g - E_{loss} \quad (3.24)$$

Finally, using the maximum short-circuit current estimated in eq 1 and the open-circuit voltage in eq 2, we can estimate a maximum theoretical limit for the efficiency as a function of the band gap of the light absorber:[58]

$$\eta(Eg) = \frac{FF * J_{SC} * V_{OC}}{P_{sum}} \quad (3.25)$$

where FF is the fill factor, defined as the ratio between the area under the J-V curve and the product $J_{SC}V_{OC}$, and P_{sun} is the total incident power, calculated as $P_{sun} = \int_0^\infty S(E)dE$, [58][60] using solar spectrum data.

CHAPTER FOUR: REASULTS AND DESCUTIONS

In this thesis DFT calculations were made by the Vienna ab initio Simulation Package (VASP) and ultrasoft pseudopotentials using Quantum-ESPRESSO code. The electronic E_{XC} energy was managed by a generalized-gradient approximation of Perdew-Burke-Ernzerhof (GGA-PBE)[3]. To get a converged global minimum energy, we performed a convergence test by varying the parameters and performing scf for the K-point grid in the Brillouin zone sampling. The Brillouin zone is sampled using the Monkhorst-Pack scheme with a grid of 7 × 7 × 1 k-points mesh for GGA functionals. Kinetic Energy cut-off (Ecutwfc), Charge density (Ecutrho), and 'relaxed' calculations for Lattice parameter. Calculated ecutwfc and ecutrho is 90 eV, and 540 eV respectively. A vacuum layer of 25 Å within the z-direction was presented to avoid interaction between the neighboring slabs, and the vdW correction (DFT-D3) that expands the structural constraints. 0.01 Ry of Gaussian smearing was used for the Brillouin zone integration.

4.1 CONVERGENCE TESTS

Convergence test is a way of optimizing the input script for a simulation to use limited computational resources efficiently. DFT obtains a result by using an iterative method, the self-consistent field (SCF) method. SCF determines ground-state electron density by calculating the energy difference with slightly changing the electron density. If the energy reaches the global minimum with achieves convergence, the calculation is finished. The convergence means the difference between the previous step and the energy is within less than a specific value (convergence threshold). Computers determine whether convergence is achieved using the set threshold. Thus, setting smaller threshold values produces more accurate results. However, an accurate input setting takes a longer time to calculate. Therefore, a convergence test is required to find a setting optimized for a model.

4.1.1 THE K-POINT OPTIMIZATION

In early computational work, when computer memory was a major limitation, the focus was on an economic choice of k-points for Brillouin zone sampling that made it possible to carry out calculations for real-space unit cells with many atoms[61]. However, for more accurate calculations, a larger set of special k-points should be used. Accurate results can be obtained by taking more grid points however, it is computationally expensive. The, scf calculations

were performed, total energy with different values of k-point grids starting from 1×1×1 to 18×18×1.

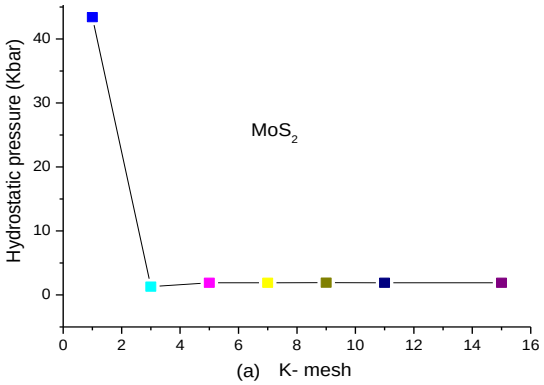

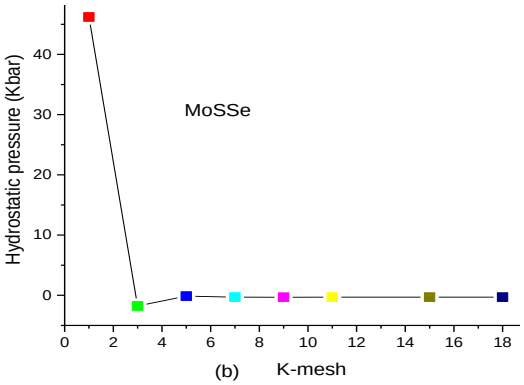

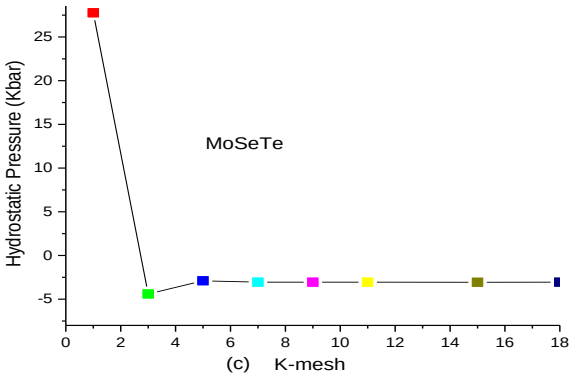

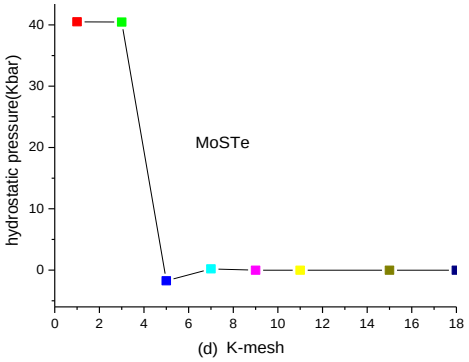

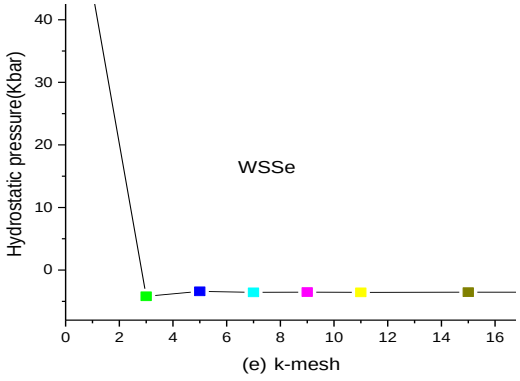

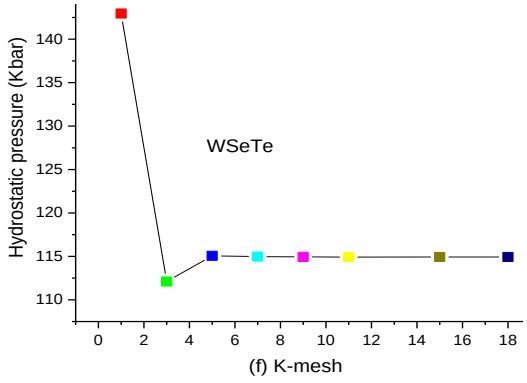

Figure 8 k-mesh vs Hydrostatic pressure for Monolayer MoS_2 (a) and MoSSe (b) MoSeTe (c) and MoSTe (d) WSSe (e) and WSeTe (f).

From figure 8 we observed the value of k mesh is changing and the hydrostatic pressure is sensitive to numerical precision, whereas total energy and others are fewer sensitive properties. Therefore, it is a good idea to monitor the hydrostatic pressure. From the graph the hydrostatic pressure is converged linearly when the k mesh values converge starting from 7*7*1, and we can continue with those values to select the proper basis set size.

4.1.2 KINETIC ENERGY CUT-OFF (ecutwfc) OPTIMIZATION.

Ecutwfc optimization was done to limit the number of plane waves with energy smaller than and/or equal to kinetic energy cutoff. This is required to computation efficiency while maintaining the accuracy of the computation result.

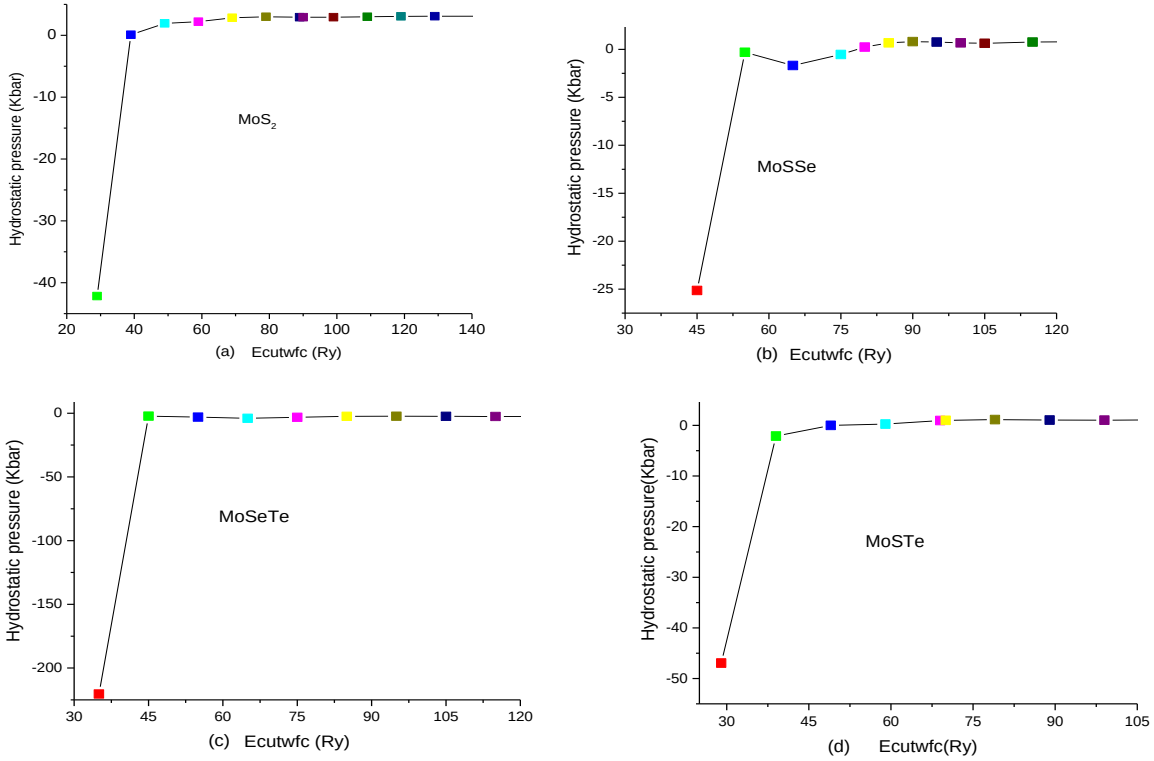

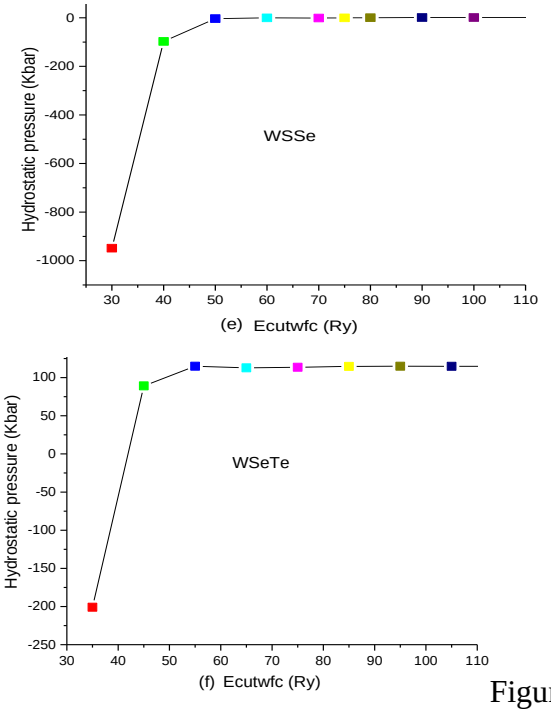

Figure 9 Ecutwfc vs Hydrostatic pressure for Monolayer MoS_2 (a), MoSSe (b), MoSeTe (c), MoSTe (d),WSSe (e), and WSeTe (f). In this study we took 90 Ry was used in the rest of the calculations.

4.1.3 CHARGE DENSITY (ecutrho) OPTIMIZATION

For the Charge density optimization a good set of values turns out to be: 7x7x1 k-mesh, ecutwfc is 90 Ry, and ecutrho 540 Ry to ensure this the hydrostatic pressure is converged to about 0 and 0.01 kbar.

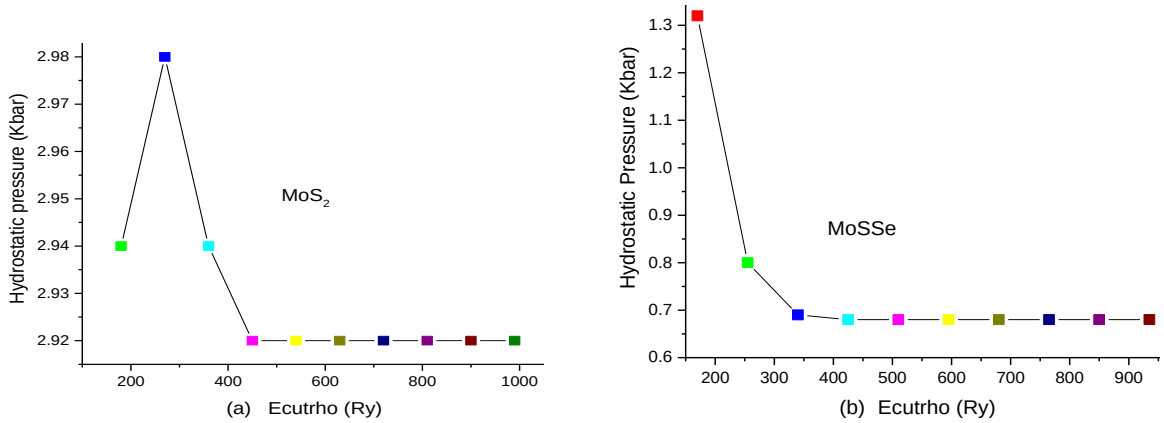

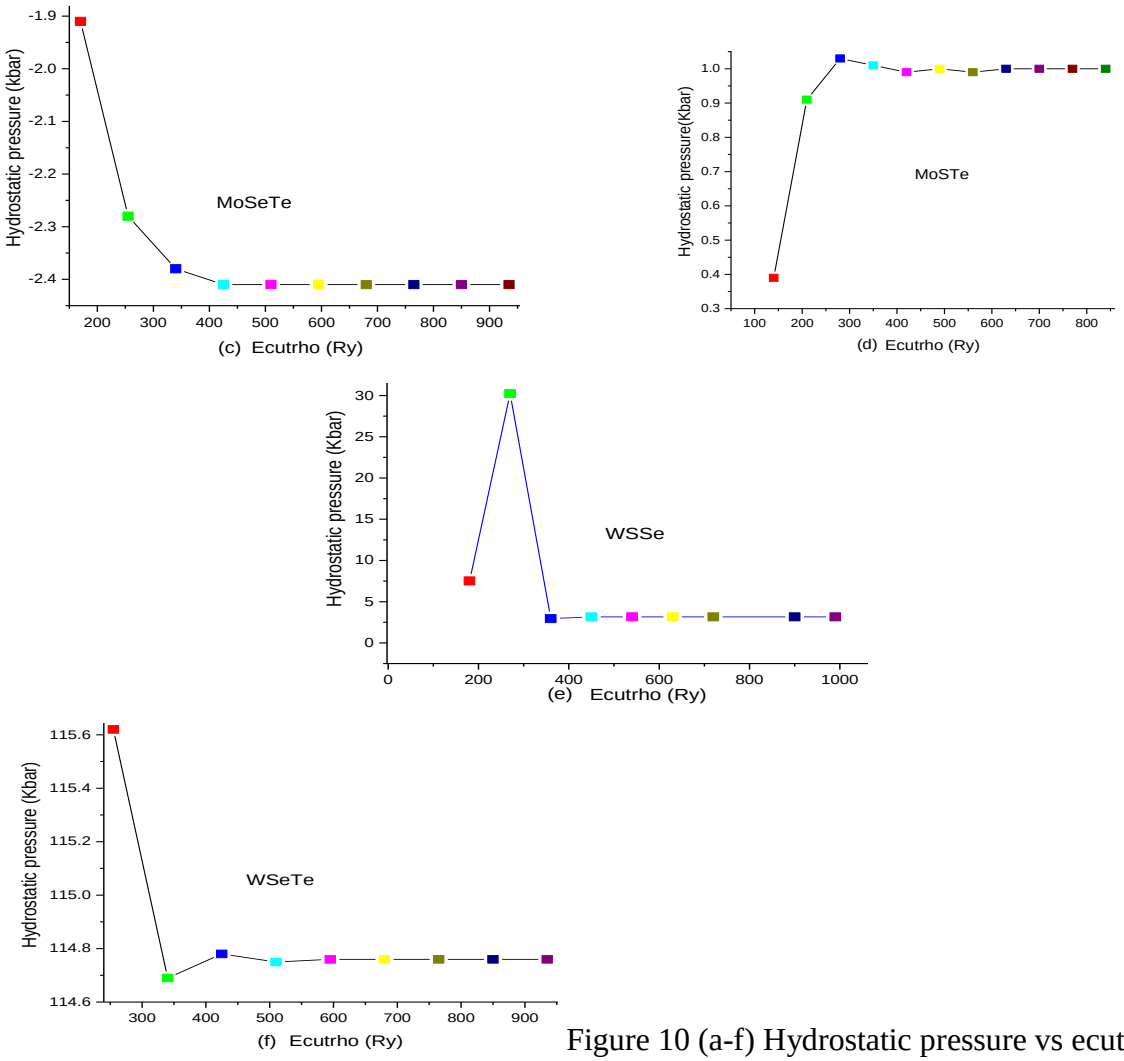

Figure 10 (a-f) Hydrostatic pressure vs ecutrho for MoS_2, MoSSe, MoSeTe, MoSTe, WSSe, and WSeTe respectively.

Figure 10 shows the convergence of Hydrostatic pressure is achieved linearly starting from 450Ry ecutrho. To get the most optimum structure taking 540 Ry is more appropriate for the rest of the calculation.

4.1.4 LATTICE CONSTANT OPTIMIZATION

Structural optimization was done by optimizing the crystal lattice constant. In this study, MoS_2, and JTMDs lattice constant optimization were done by giving the initial lattice constant (a0) smaller than the expected value in the calculation of its total energy. The calculations were repeated where at the end of each step we obtained the new lattice constants (a1) and the new total energy (E1). The iteration continued until we gained the lowest total energy.

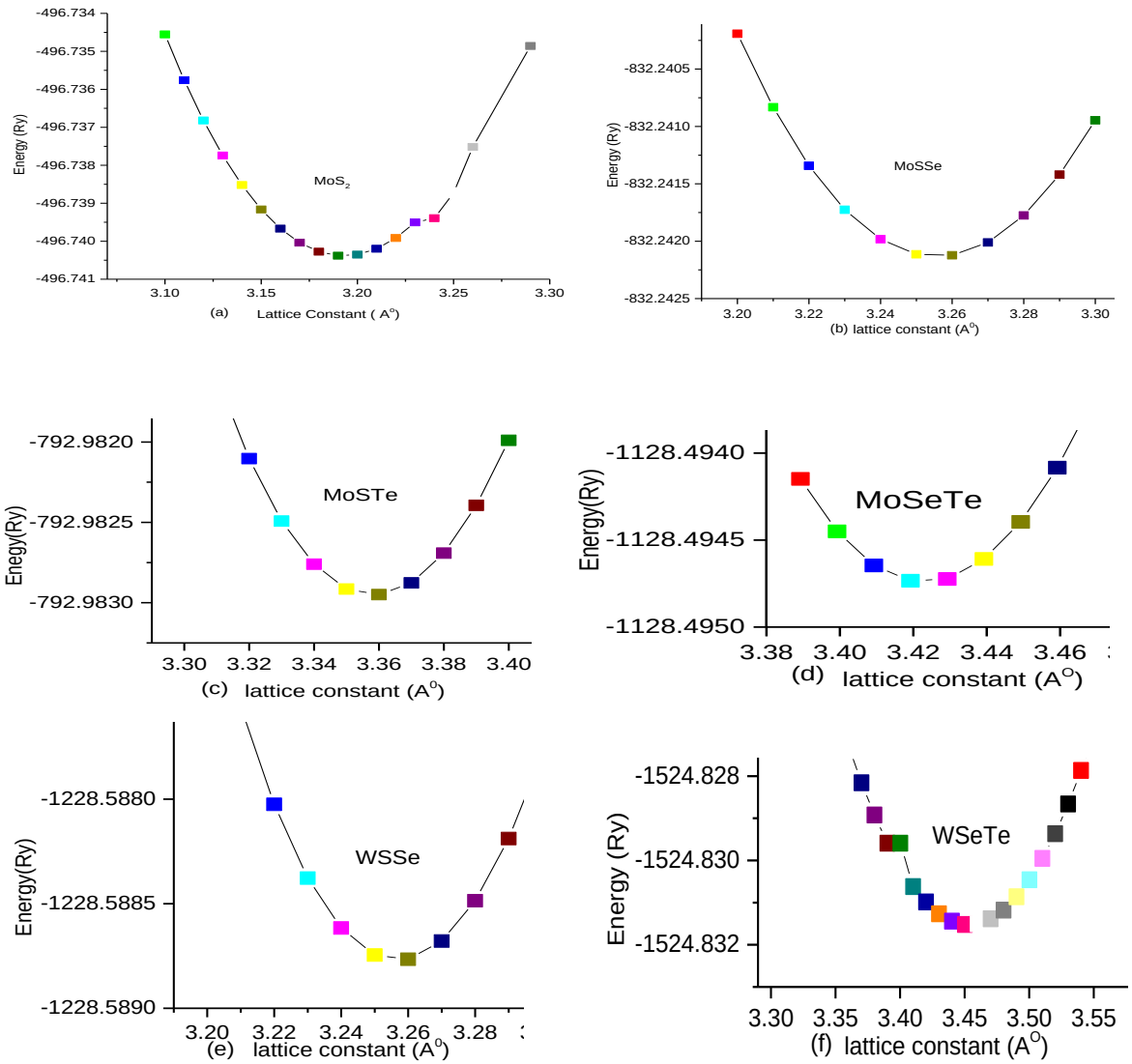

Figure 11 (a-f) Equilibrium lattice parameter of Monolayer, (MoS_2, MoSSe, MoSTe, MoSeTe, WSSe, and WSeTe) respectively. Figure 11 shows that the optimized lattice parameter is (3.19Å, 3.26Å, 3.36Å, 3.41Å, 3.26Å, and 3.45Å) for (MoS_2, MoSSe, MoSTe, MoSeTe, WSSe, and WSeTe) respectively.

4.2 STRUCTURAL OPTIMIZATION OF TMD AND JTMDS MONOLAYERS

The lattice mismatch between JTMDs and MoS_2 monolayers was calculated and is presented in Table2, and Optimized lattice constants were all following previous results. The mismatch calculation using the formula:

$$\text{Lattice mismatch (\%)} = \frac{\left(\text{JTMDs}\left(\text{Lattice Parameter a(Å)}\right) - \text{MoS2}\left(\text{Parameter a(Å)}\right)\right) * 100\%}{\text{JTMDs}\left(\text{Lattice Parameter a(Å)}\right)}$$

The structural properties of JTMDs heterostructures are determined by the lattice parameter mismatch, growth conditions, and growth techniques. Multilayer vdWH are a promising way of combining different 2D materials to achieve desirable properties for numerous TMDs in which individual covalently bonded layers are held together by weekly vdWH forces without dangling bonds, have a unique advantage.

Table 2 Optimized lattice constants within lattice mismatch values

MXY	Calculated lattice constant a(Å)	References lattice constant a(Å)	Calculated mismatch values (%)
MoS_2	3.19	3.19[62],3.19[28]	
MoSSe	3.26	3.25[63],3.26[64]	2.147
MoSTe	3.36	3.35[38],3.36[65]	5.059
MoSeTe	3.41	3.42[38],3.41[66]	6.725
WSSe	3.26	3.26[67],3.26[68]	2.147
WSeTe	3.45	3.42[38],3.45[69]	7.536

An optimized lattice parameter of WSSe, MoSSe, and MoSTe less than 5.059% mismatch values are appropriate to form heterostructures with MoS_2. Due to similarly optimized lattice constants of MoSSe, MoSTe, and WSSe with MoS_2, new 2D heterostructures of a JTMD (MoSSe or MoSTe or WSSe) were created, and MoS_2 monolayers were designed according to the first principle calculations.

4.3 ELECTRONIC PROPERTIES OF TMD AND $JTMD_S$ MONOLAYERS

The bandgap of 2D materials is an important parameter for potential electronic and optoelectronic applications. The band-gap values of MoS_2, WSSe, MoSSe, and MoSTe monolayers calculated by the GGA-PBE exchange-correlation function are shown in Figure 11,a-d. The calculated band gap of MoS_2, MoSSe, MoSTe, and WSSe is (1.74 eV, 1.65 eV,

1.16 eV, and 1.77 eV), respectively. A direct bandgap was observed for MoS_2, WSSe, and MoSSe, and an indirect bandgap was shown for MoSTe monolayer.

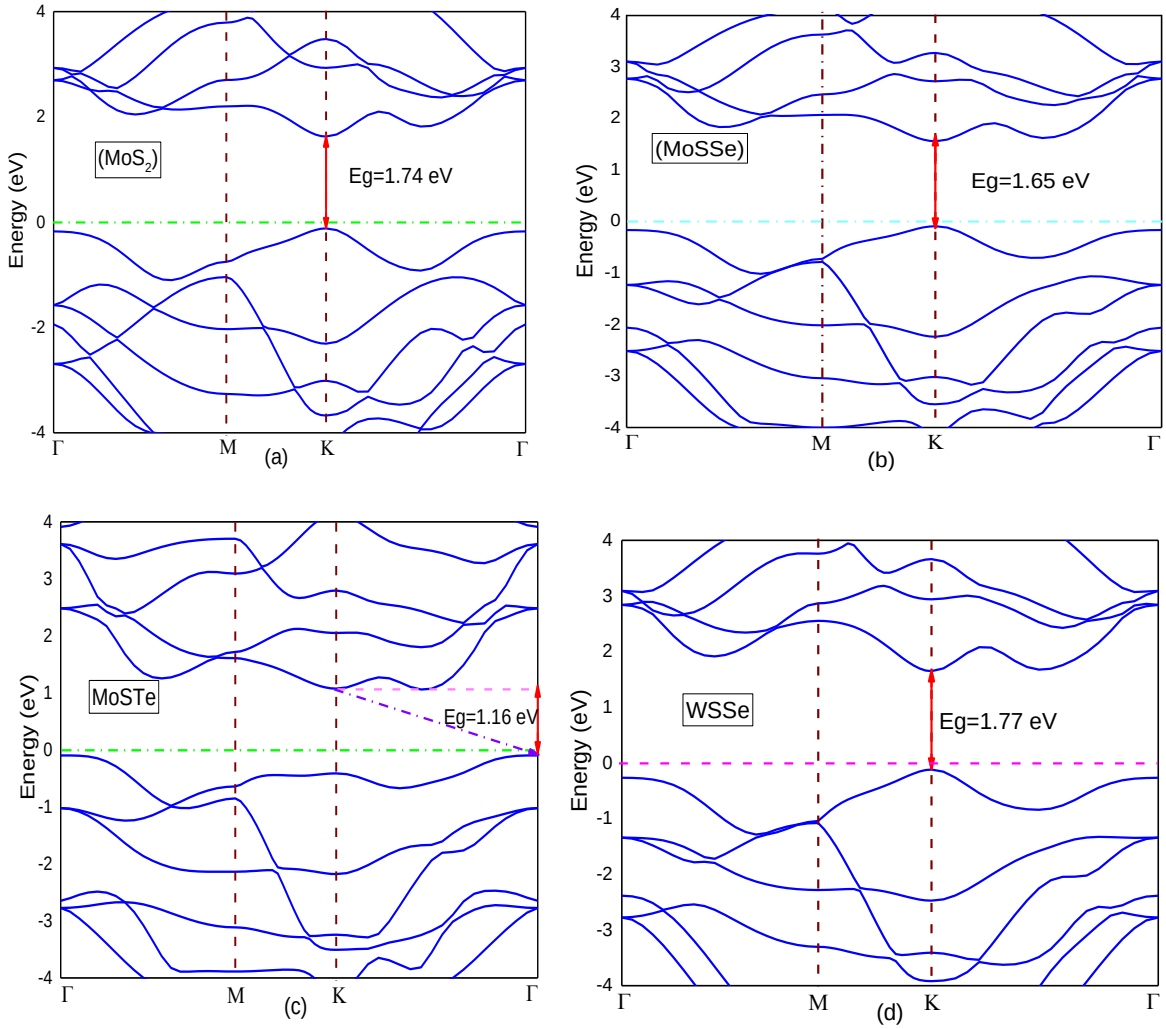

Figure 12 the electronic band structure of monolayers

From figure 12 it can be seen that the CBM and VBM of monolayer MoS_2, MoSSe, and WSSe are located at the K-point in the Brillouin zone, while for monolayer MoSTe the CBM is positioned between K- Γ path and the VBM is at the Γ-point. This result is consistent with previous research[70][71][72].

PDOS were plotted for MoS_2, Janus MoSSe, MoSTe, and WSSe monolayer results as shown in Figure13. a-d.

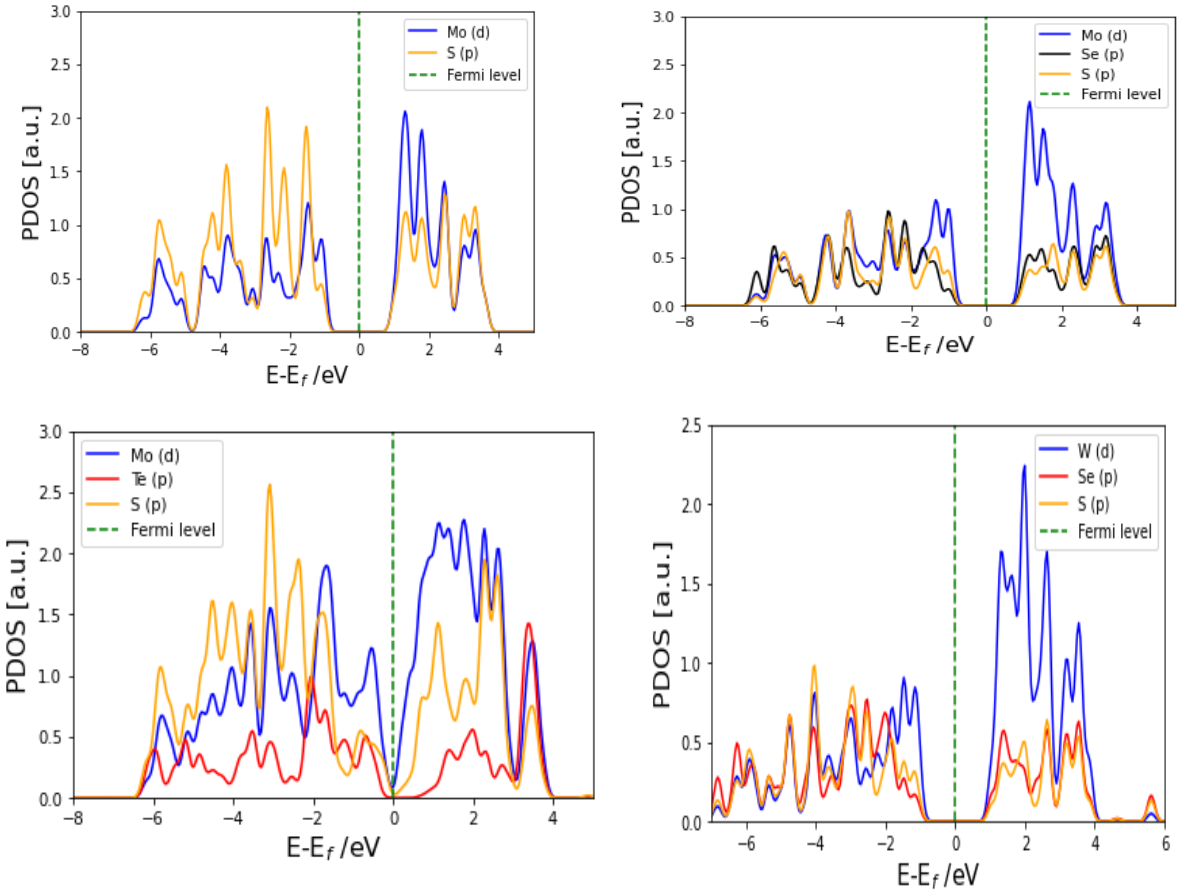

Figure 13The PDOS of monolayer MoS_2, MoSSe, MoSTe, and WSSe

The states of MoS_2, MoSSe, and MoSTe near the fermi level the CBM and VBM is dominated by Mo-4d atoms, whereas WSSe highly contributed from W-4d atoms.

4.4 JTMD/MoS_2 OPTIMIZED HETEROSTRUCTURES

To know the most optimum Heterostructures performed eight main stacking patterns of the structures, and their structures were initially optimized as brief in Table 3. This work, chose the AAII-S stacking mode for the heterostructures MoSSe/MoS_2, WSSe/MoS_2, and

$MoSTe/MoS_2$, the most negative binding energy which has been established to be more stable than the other stacking modes. The most stable heterostructures required most negative binding energy, optimized lattice constant, and the appropriate interlayer distance.

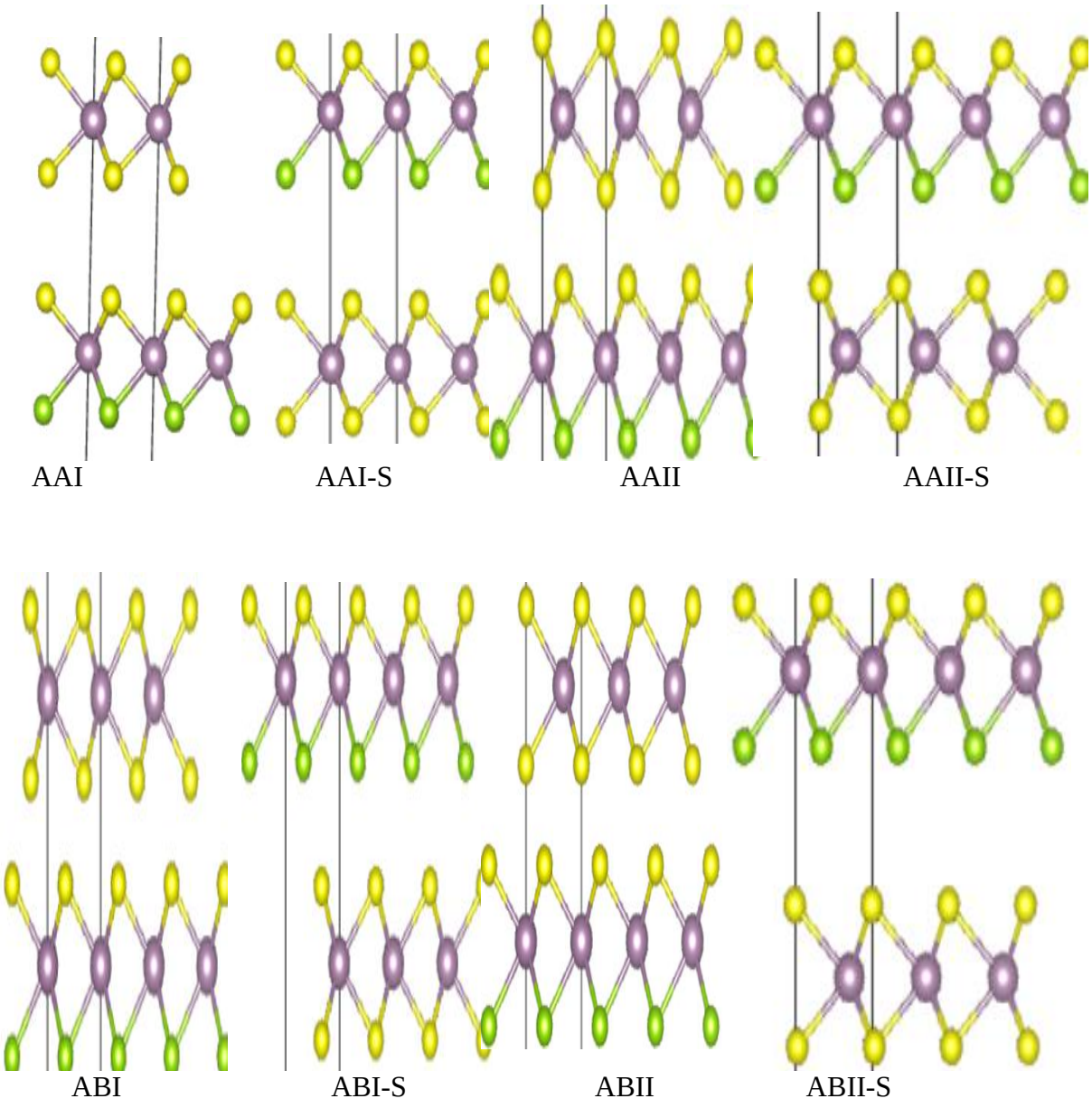

Figure 14 a side view

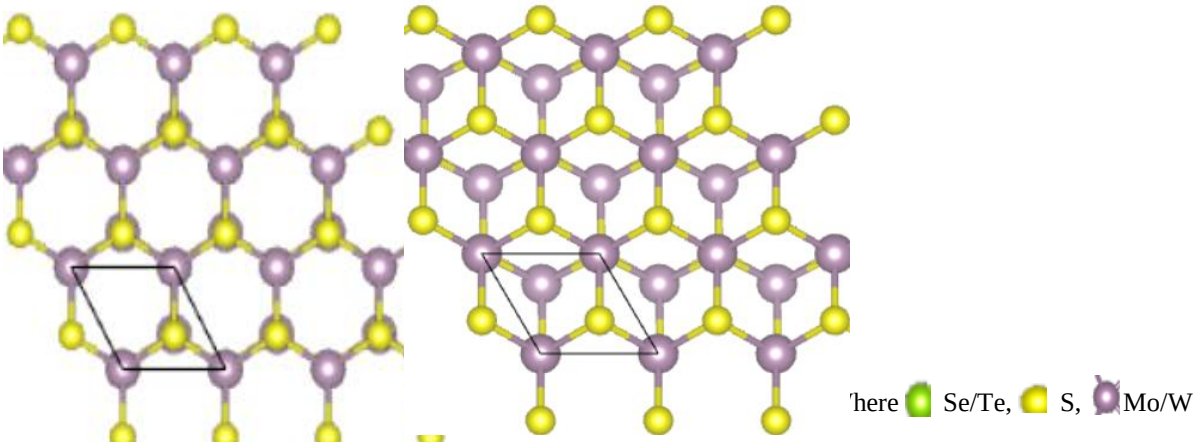

Figure 14 b Top views

Figure (14 a -b) Side and Top view of different stacking hetro-bilayer configurations.

In $MoSSe/MoS_2$, $MoSTe/MoS_2$, and $WSSe/MoS_2$ configurations AAI, the atoms S/Se/Te of Janus monolayer located below the S atoms of MoS_2, and Mo/W atoms of Janus monolayer below Mo atom of MoS_2. In configuration AAI-S, the atoms S/Se/Te of Janus monolayer are located above the S atoms of MoS_2, and Mo/W atoms of Janus monolayer above Mo atom of MoS_2.In the case of AAII, configuration, of the Janus W/Mo atoms above MoS_2 of the S atoms, and S atoms of the Janus below Mo atom of MoS_2. In AAII-S formations, the atoms of Mo/W above the S atoms of MoS_2, and Se/Te atoms of Janus above Mo atom of MoS_2. In the ABI staking the W/Mo atoms of the Janus below the Mo atoms of MoS_2. In the case of ABI-S configuration the Mo/W atoms of Janus monolayer above the Mo atoms of MoS_2. In the ABII configuration, the S atom of monolayer MoS_2 above the Mo/W atoms of Janus monolayers. In the last configuration ABII-S configuration the Mo/W atoms of Janus monolayer above the S atoms of monolayer MoS_2.

Table 3 Optimized lattice constant a(Å), Interlayer distance d(Å), and Binding energy (eV) for different stacking patterns of the heterostructure.

Heterostructure	Staking pattern	Optimized lattice constant a(Å)	Interlayer Distance d(Å)	Binding Energy E_b (eV)
	AAI	3.220	3.75994	−0.00627001
$MoSSe/MoS_2$	AAI-S	3.220	3.75994	−0.00627001
	AAII	3.220	2.73059	−0.0094165
	AAII-S	3.220	3.08983	−0.01134065
	ABI	3.240	3.62043	−0.00843097
	ABI-S	3.230	3.72712	−0.00995421
	ABII	3.230	3.59398	−0.00947932
	ABII-S	3.220	3.63213	−0.01128177
$MoSTe/MoS_2$	AAI	3.270	3.69406	0.0008927
	AAI-S	3.270	3.50528	−0.00176342
	AAII	3.270	3.64429	−0.00338643
	AAII-S	3.270	3.77629	−0.00862683
	ABI	3.280	3.61412	−0.00308244
	ABI-S	3.280	3.85562	−0.00606722
	ABII	3.270	3.59376	−0.00366361
	ABII-S	3.270	3.76159	−0.00825678
	AAI	3.220	3.55967	−0.00789039
$WSSe/MoS_2$	AAI-S	3.220	3.70606	−0.00874931
	AAII	3.220	3.52090	−0.01335095
	AAII-S	3.220	3.63358	−0.01483285
	ABI	3.240	3.53494	−0.01154163
	ABI-S	3.240	3.64507	−0.01287585
	ABII	3.230	3.08973	−0.01336809
	ABII-S	3.230	3.60498	−0.01477089

The Optimized lattice constant, interlayer distance, and the binding energies of different stacking models of MoSSe, MoSTe, and WSSe on the MoS_2 monolayer of the heterostructures, are calculated and analyzed are listed in Table 3. To quantitatively evaluate the binding energy between heterostructures, JTMDs, and MoS_2 monolayer atoms, we first calculated the optimum energy of each monolayer and the heterostructures, then calculated the binding energy using the following formula:

$$E_b = E_{HRS} - E_{JTMD1} - E_{TMD2}$$

where E_b is binding energy, E_{HRS} is total energy of heterostructures, E_{JTMD1} is total energy of the Janus monolayer and E_{TMD2} is total energy of MoS_2 monolayer.

Except for MoSTe/MoS_2 AAI stacking mode, the remaining stacking configuration has negative binding energy used to form a heterostructure. The configurations, AAI of MoSTe/MoS_2 show positive binding energy which is difficult to form heterostructure from MoSTe and MoS_2 monolayer. The negative binding energy in the JTMDs/MoS_2 heterostructures is a good indicator of weak vdW forces that bound JTMDs with the MoS_2 monolayer.

4.5 JTMDs/MoS_2 HETEROSTRUCTURES PHOTOCATALYST MATERIALS FOR WATER SPLITTING

To align the energy levels for the various materials, their vacuum levels are set to zero. For the water-splitting reaction, the commonly used values of the standard reduction potential for H^+/H_2 and the oxidation potential for O_2/H_2O are -4.44 and -5.67 eV, respectively[40]. It is well known that the oxidation and reduction abilities are measured by the VBM energy and CBM energy, respectively. In this study configuration AAII-S of MoSSe/MoS_2, MoSTe/MoS_2, and WSSe/MoS_2, heterostructures the CBM, -4.838, -5.590, -4.809 eV and VBM are located at, -5.865, -5.894, and-5.646 respectively. Comparing with the water redox potentials, the CBM of MoSSe/MoS_2, MoSTe/MoS_2, and WSSe/MoS_2, heterostructure is located at 0.398, 1.15, and 0.369 eV, respectively just below the reduction potential of H^+/H_2. Comparing with the water oxidation potentials, the VBM of WSSe/MoS_2, heterostructure is located at -0.024 eV above, and heterobilayer MoSSe/MoS_2, and

$MoSTe/MoS_2$ are located at 0.195, and 0.224 eV just below the oxidation potential of O_2/H_2O respectively.

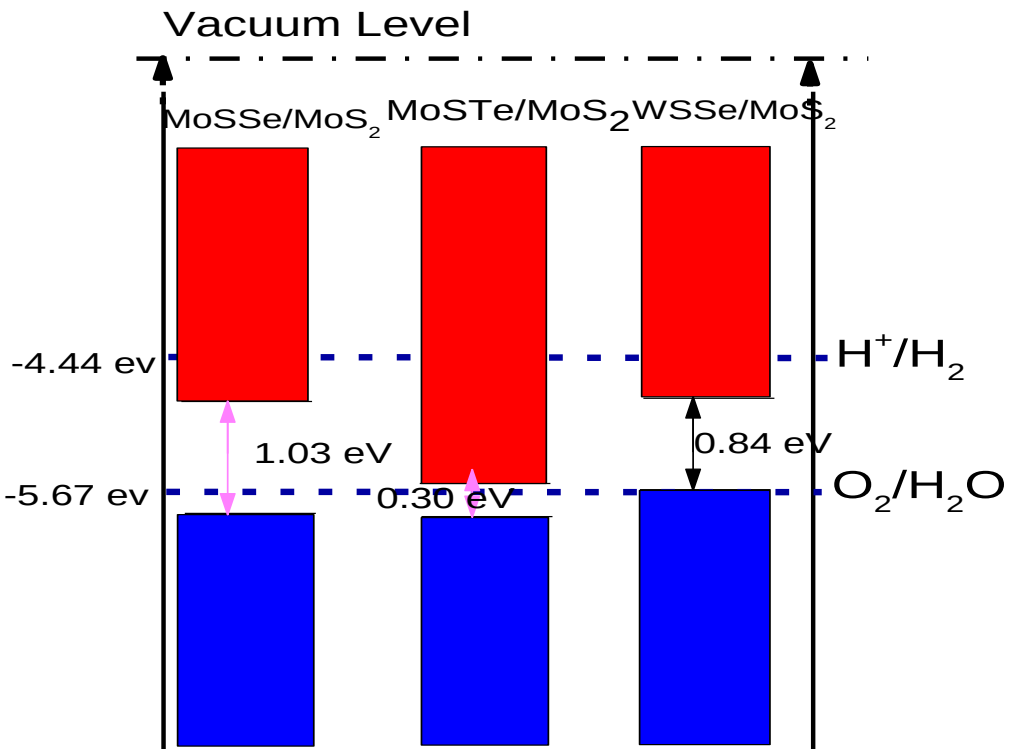

Figure 15 Band edge positions of AAII-S for $MoSSe/MoS_2$,$MoSTe/MoS_2$,and $WSSe/MoS_2$

Heterostructure with reference to the water redox potentials of H^+/H_2 and O_2/H_2O at pH =0.Compared with the water redox and oxidation potentials, of heterostructures, $MoSSe/MoS_2$, $MoSTe/MoS_2$, and $WSSe/MoS_2$, are incapable of photocatalyst materials for full water splitting. Compared with the water oxidation potentials $MoSSe/MoS_2$, and $MoSTe/MoS_2$ heterostructures are located lower than the oxidation potential of O_2/H_2O, making them appropriate for oxygen evolution reaction (OER). Compared with the water redox potentials of $MoSSe/MoS_2$, $MoSTe/MoS_2$, and $WSSe/MoS_2$, heterostructures are located just below the reduction potential of H^+/H_2, which is inappropriate for the hydrogen evolution reaction (HER)

4.6 ELECTRONIC PROPERTIES OF JTMDS WITH MOS_2 MONOLAYER

The electrical properties of monolayers and heterostructures for each staking are calculated

by GGA-PBE is presented in Table 4. We also employed the work function to clarify the charge transfer between the interfaces, based on the following equation:

Work function, φ [eV] = Vacuum level - Fermi energy (4.1)

Table 4 Electrical properties of JTMDs monolayers and JTMDs/MoS_2 heterostructures using GGA-PBE

TMD & JTMD/MoS_2	E_g [eV]	Fermi energy [eV]	Vacuum-Level (eV)	Electron affinity [eV]	Ionization Energy (eV)	Work function, φ [eV]
MoS_2	1.744 (dir)	-2.268757	3.528	-4.169	-5.913	5.797
MoSSe	1.645 (dir)	-1.361654	4.421	-4.234	-5.880	5.783
MoSTe	1.157 (ind)	-0.380833	5.216	-4.555	-5.711	5.597
WSSe	1.768 (dir)	-1.575334	3.960	-3.885	-5.653	5.535
MoSSe/ MoS_2	1.026 (ind)	0.738898	6.506	-4.838	-5.865	5.767
MoSTe/MoS_2	0.303 (ind)	1.481600	7.223	-5.590	-5.894	5.741
WSSe / MoS_2	0.838 (dir)	0.590545	6.144	-4.809	-5.646	5.553

The JTMDs/MoS_2 heterostructures electronic band structures for different configurations along with the monolayers MoS_2 and JTMDs are studied and demonstrated in Fig.(15 a-c). The projected band structures of the MoSSe/MoS_2, and MoSTe/MoS_2 heterostructures configuration-AAII-S are revealed in Figure 16 (a & c). It can be clearly seen that the CBM and VBM is located at the K, and Γ point in the Brillouin zone respectively, whereas for WSSe/MoS_2 heterostructure shown in fig.(16 c) both CBM and VBM are positioned at the K point in the Brillouin zone.

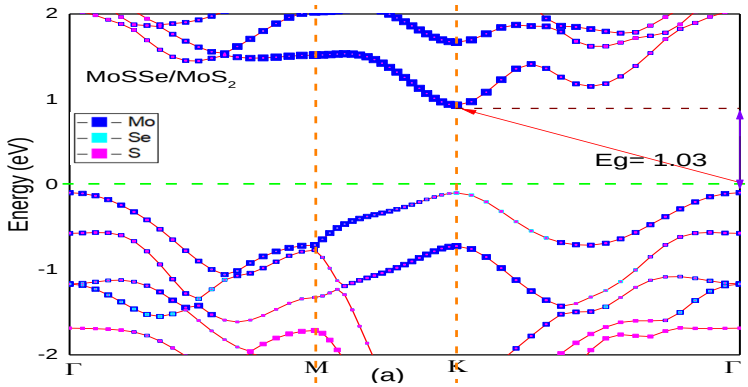

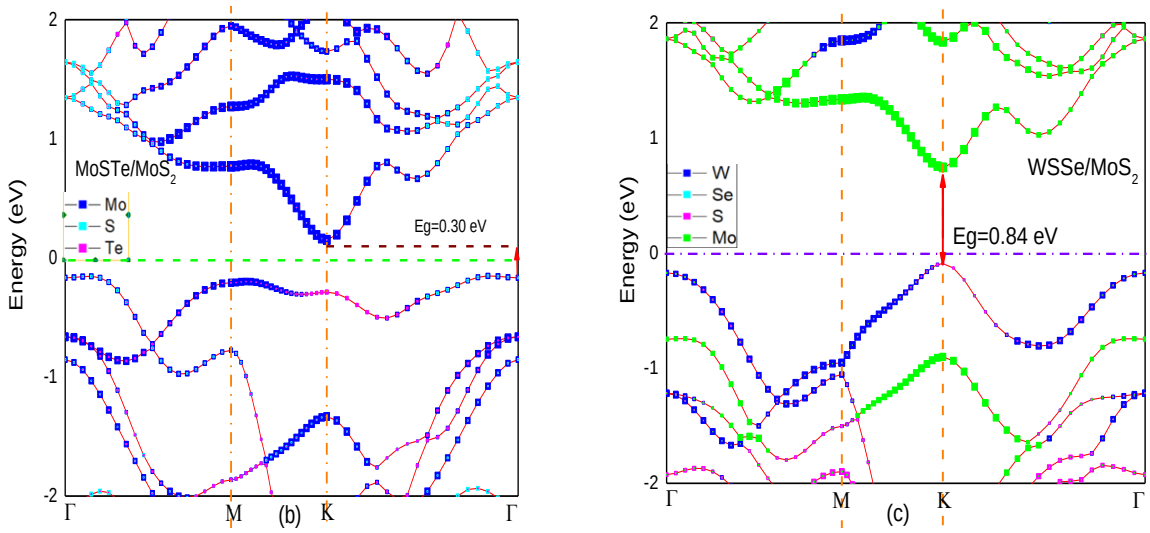

Figure 16 Projected Band Structure of heterostructures $MoSSe/MoS_2$ (a), $MoSTe/MoS_2$ (b),and $WSSe/MoS_2$ (c).

The states of $WSSe/MoS_2$ near the Fermi level the CBM is dominated by Mo-4d,and the VBM is dominated by W-4d atoms, whereas the states of $MoSSe/MoS_2$, and $MoSTe/MoS_2$near the Fermi level their CBM and VBM are dominated by Mo-4d.

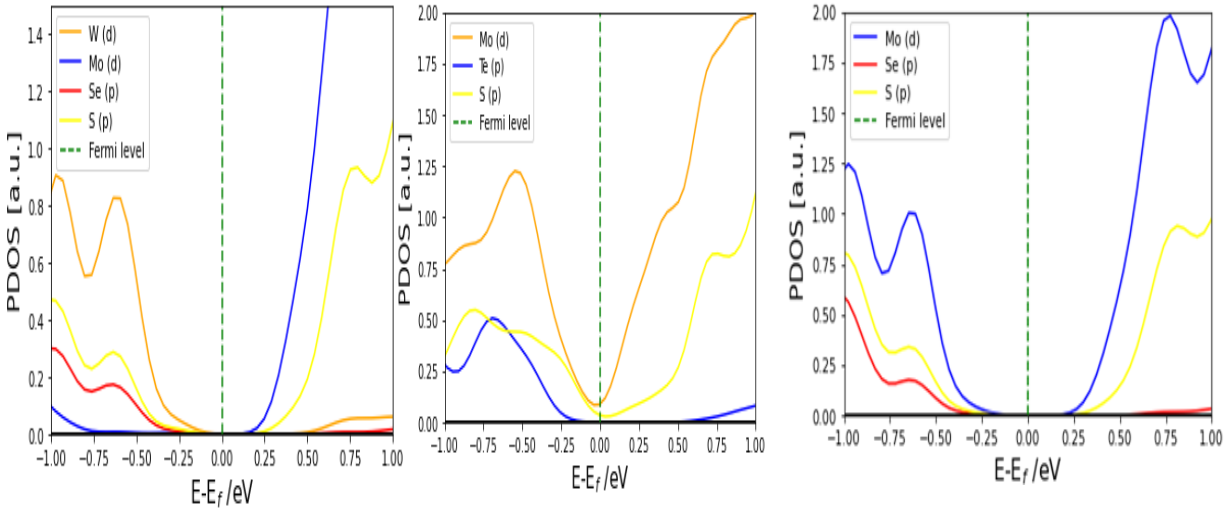

Figure 17 PDOS of $WSSe/MoS_2$, $MoSTe/MoS_2$ and $MoSSe/MoS_2$ heterostructures.

In the MoS_2/WSSe heterostructure, which is type-II band alignment the migration of charge carriers in the MoS_2/WSSe heterostructures can occur in three different ways as shown in figure18.

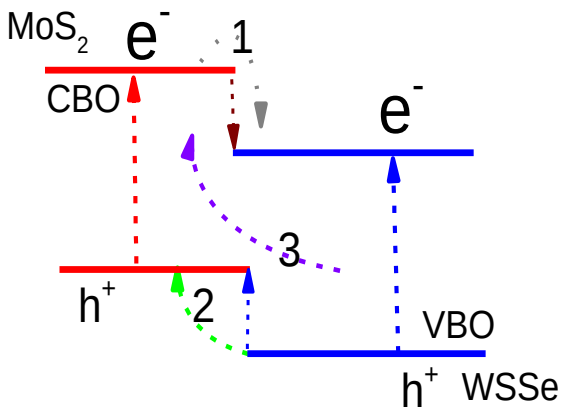

Figure 18 Migration of photogenerated carriers at the MoS_2/WSSe interface.

(1) Driven by the conduction-band offset (CBO) of 0.065 eV, the create electron, in the conduction-band minimum of the MoS_2 layer can be transferred to the conduction-band minimum of the WSSe layer. (2) The existence of the VBO of 0.164 eV, the photogenerated holes in the valency-band maximum of the WSSe layer can be promptly moved to the VBM of the MoS_2 layer. (3) Finally the third type of migration is the unwanted recombination of photogenerated carriers. In addition, one can anticipate that the charge transfers between the MoS_2 and WSSe layers can generate a polarized electric field at the interface, which will prevent the photogenerated carriers from recombination via path 3 depicted in Figure 18 and encourage them to migrate through paths 1 and 2.

In this study, Janus MoSSe/MoS_2, MoSTe/MoS_2, and WSSe/MoS_2 heterostructures, the CBM are localized on the MoS_2 and VBM on the MoSSe, MoSTe, and WSSe respectively. Based on the calculated result as showing in Figure 19 MoSSe/MoS_2, MoSTe/MoS_2 are of type-I and WSSe/MoS_2 type-II band alignment. In type-II (staggered gap) heterojunctions, the VBM and the CBM belong to two separate components with different work functions, Ionization Energy, and Electron affinity.

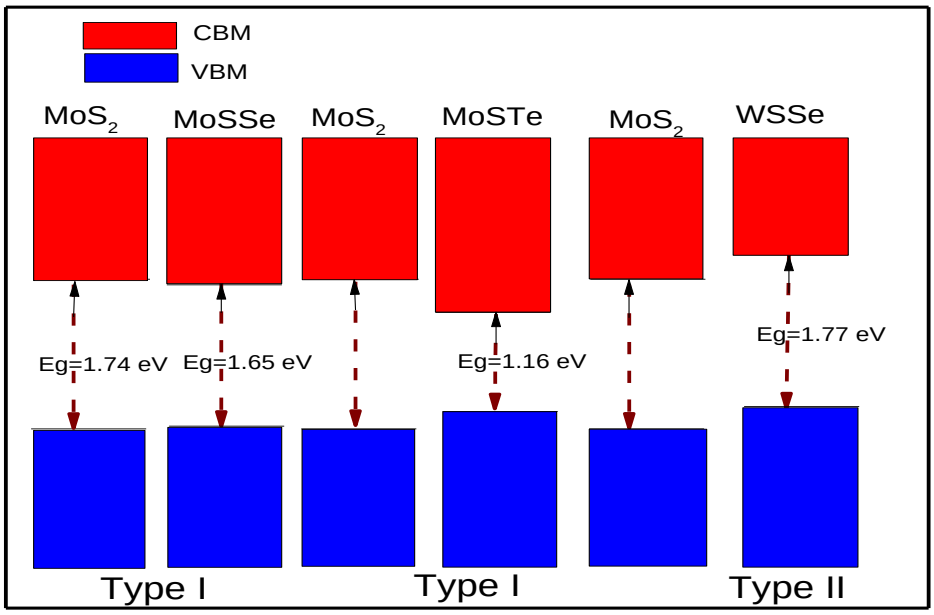

Figure 19 Band alignment illustrations of type-I($MoSSe/MoS_2$, $MoSTe/MoS_2$) and type-II ($WSSe/MoS_2$) heterostructures.

The bandgap of JTMD monolayers calculated by the PBE functional ~0.5 eV correspondingly smaller than that of the HSE06 functional, and the use of SOC leads to the bandgap reduction by 0.1~0.4 eV due to the band splitting induced by the SOC[38].

The bandgap of $MoSSe/MoS_2$ and $WSSe/MoS_2$ vdW heterobilayer calculated by PBE functional have indirect and direct with configuration AAII-S of 1.03 eV and 0.84 eV, respectively as shown in Table 4. Calculated bandgap values are approximately similar to the model bandgap for achieving the maximum thermodynamically possible conversion efficiency of sunlight to electricity is around 1.3 eV to 2.2 eV, which is optimal for a photovoltaic application in solar cells. Conversely, $MoSTe/MoS_2$ heterobilayer possesses too small an indirect bandgap (0.303eV) to inefficiently produce the visible light portion of the solar spectrum.

4.7 THEORETICAL EFFICIENCY LIMIT OF JTMDs/MoS_2 HETEROSTRUCTURES SEMICONDUCTOR SOLAR CELLS.

The interface band alignment between donor and acceptor materials is critical to the maximum PCE. From the band alignment as shown in Figure 19, the conduction band offset (CBO) of $MoSSe/MoS_2$, $MoSTe/MoS_2$, and $WSSe/MoS_2$ is 0.065, 0.386,and 0.284 eV respectively. Fill factor for all heterostructures are set at 0.57 and 0.3 eV is the empirical

approximation of kinetic energy conversion loss. This study calculated the power conversion efficiency of $MoSSe/MoS_2$, $MoSTe/MoS_2$,and $WSSe/MoS_2$ heterostructure were 19.41%, 0.12%, and 16.25% respectively. Additionally, we find that $WSSe/MoS_2$ shows desirable type II band alignment for constructing highly efficient heterojunction solar cells with strong charge separation and enhanced sunlight absorption. In particular, the calculated maximum power conversion efficiency (PCE) of our designed $MoSSe/MoS_2$ and $WSSe/MoS_2$ heterostructure solar cells can reach as high as 19.41%, and 16.25%, respectively.

5 CONCLUSIONS AND RECOMMENDATIONS

5.1 CONCLUSIONS

In summary, the study theoretically using DFT, the structural stability, electronic properties, and photocatalytic performance for water splitting of JTMDs/MoS_2 heterostructures. The calculated direct bandgap is 0.84 and indirect bandgap 1.03, 0.30 eV for WSSe/MoS_2, and MoSSe/MoS_2, MoSTe/MoS_2 respectively. In this thesis, Janus WSSe/MoS_2, vdW heterostructure resulting in type-II band alignment. Compared with the water redox and oxidation potentials, of heterostructures, MoSSe/MoS_2, MoSTe/MoS_2, and WSSe/MoS_2, are unable to photocatalyst materials for fully use water splitting. MoSSe/MoS_2 heterobilayer with type-I band alignment and WSSe/MoS_2 vdW heterobilayer with type-II band alignment is calculated, making them promising candidates for PV applications. Conversely, MoSTe/MoS_2 heterobilayer which has type-I band alignment possesses too small a bandgap to utilize the visible light portion of the solar spectrum inefficiently. The bandgap of MoSSe/MoS_2 and WSSe/MoS_2 vdW heterobilayer calculated by PBE functional have indirect and direct of 1.03, and 0.84 eV respectively. These calculated bandgap values are approximately similar to the model bandgap for achieving the maximum thermodynamically possible conversion efficiency of sunlight to electricity is around 1.3 eV to 2.2 eV, which is optimal for a photovoltaic application in solar cells. The designed power conversion efficiency of MoSSe/MoS_2 is (19.41%) and WSSe/MoS_2 is (16.25%).

5.2 RECOMMENDATIONS

The following points are recommended for further study: In this research, JTMDs/MoS_2 heterostructures showed many interesting properties. The JTMDs/MoS_2 heterostructure calculated by the PBE functional which underestimate the bandgap values than that of the HSE06 functional. In the future, the heterostructures can be studied using HSE06 to get better energy applications. Additionally, we need to calculate charge carrier mobility and the thermal stabilities of heterostructures for completeness. Further studies are also recommended to modulate the MoSTe/MoS_2 heterostructure by doping other heavy elements to create stress in the structure and improve its electronic and photocatalyst properties. Nowadays theoretical material engineering has grown very fast, consequently it is better to bring experimental works and theoretical modeling features together to understand and study their efficiency and performance of Janus transition metal dichalcogenides for photovoltaic and photocatalyst water splitting applications.

REFERENCES

[1] M. I. and N. M. R. Pech-canul, *Semiconductors Synthesis, Properties and Applications*. 2019.

[2] A. Kudo and Y. Miseki, "Heterogeneous photocatalyst materials for water splitting," *Chem. Soc. Rev.*, vol. 38, no. 1, pp. 253–278, 2009, doi: 10.1039/b800489g.

[3] D. R. Chowdhury, L. Spiccia, S. S. Amritphale, A. Paul, and A. Singh, "A robust iron oxyhydroxide water oxidation catalyst operating under near neutral and alkaline conditions," *J. Mater. Chem. A*, vol. 4, no. 10, pp. 3655–3660, 2016, doi: 10.1039/c6ta00313c.

[4] F. M. Altincicek, "Synthesis And Characterization Of Quasi-Two- Dimensional Chromium Sulfides," no. January, 2019, doi: 10.13140/RG.2.2.14154.82885.

[5] Y. Jing, B. Liu, X. Zhu, F. Ouyang, J. Sun, and Y. Zhou, "Tunable electronic structure of two-dimensional transition metal chalcogenides for optoelectronic applications," *Nanophotonics*, vol. 9, no. 7, pp. 1675–1694, 2020, doi: 10.1515/nanoph-2019-0574.

[6] M. Bernardi, M. Palummo, and J. C. Grossman, "Extraordinary sunlight absorption and one nanometer thick photovoltaics using two-dimensional monolayer materials," *Nano Lett.*, vol. 13, no. 8, pp. 3664–3670, 2013, doi: 10.1021/nl401544y.

[7] T. Tan, X. Jiang, C. Wang, B. Yao, and H. Zhang, "2D Material Optoelectronics for Information Functional Device Applications: Status and Challenges," *Adv. Sci.*, vol. 7, no. 11, 2020, doi: 10.1002/advs.202000058.

[8] X. Li *et al.*, "Graphene and related two-dimensional materials: Structure-property relationships for electronics and optoelectronics," *Appl. Phys. Rev.*, vol. 4, no. 2, 2017, doi: 10.1063/1.4983646.

[9] M. Huang, S. Li, Z. Zhang, X. Xiong, X. Li, and Y. Wu, "Multifunctional high-performance van der Waals heterostructures," *Nat. Nanotechnol.*, vol. 12, no. 12, pp. 1148–1154, 2017, doi: 10.1038/NNANO.2017.208.

[10] L. F. Mattheiss, "Band structures of transition-metal-dichalcogenide layer compounds," *Phys. Rev. B*, vol. 8, no. 8, pp. 3719–3740, 1973, doi: 10.1103/PhysRevB.8.3719.

[11] R. Ramirez and M. C. Böhm, "Band Structures of Intercalation Compounds. The System (NH4)(NH3)3(TiS2)4," *Zeitschrift fur Naturforsch. - Sect. A J. Phys. Sci.*, vol. 42, no. 11, pp. 1346–1356, 1987, doi: 10.1515/zna-1987-1119.

[12] Q. H. Wang, K. Kalantar-Zadeh, A. Kis, J. N. Coleman, and M. S. Strano, "Electronics and optoelectronics of two-dimensional transition metal dichalcogenides," *Nat. Nanotechnol.*, vol. 7, no. 11, pp. 699–712, 2012, doi: 10.1038/nnano.2012.193.

[13] C. Zhang *et al.*, "Systematic study of electronic structure and band alignment of monolayer transition metal dichalcogenides in Van der Waals heterostructures," *2D Mater.*, vol. 4, no. 1,

pp. 1–10, 2017, doi: 10.1088/2053-1583/4/1/015026.

[14] X. Duan, C. Wang, A. Pan, R. Yu, and X. Duan, "Two-dimensional transition metal dichalcogenides as atomically thin semiconductors: Opportunities and challenges," *Chem. Soc. Rev.*, vol. 44, no. 24, pp. 8859–8876, 2015, doi: 10.1039/c5cs00507h.

[15] H. Xu, D. He, M. Fu, W. Wang, H. Wu, and Y. Wang, "Optical identification of MoS_2/graphene heterostructure on SiO_2/Si substrate," *Opt. Express*, vol. 22, no. 13, p. 15969, 2014, doi: 10.1364/oe.22.015969.

[16] C. Lan, Z. Shi, R. Cao, C. Li, and H. Zhang, "2D materials beyond graphene toward Si integrated infrared optoelectronic devices," *Nanoscale*, vol. 12, no. 22, pp. 11784–11807, 2020, doi: 10.1039/d0nr02574g.

[17] J. Wang and B. Liu, "Electronic and optoelectronic applications of solution-processed two-dimensional materials," *Sci. Technol. Adv. Mater.*, vol. 20, no. 1, pp. 992–1009, 2019, doi: 10.1080/14686996.2019.1669220.

[18] M. Ye, D. Zhang, and Y. K. Yap, "Recent advances in electronic and optoelectronic devices based on two-dimensional transition metal dichalcogenides," *Electron.*, vol. 6, no. 2, 2017, doi: 10.3390/electronics6020043.

[19] H. Li, Y. Shi, M. H. Chiu, and L. J. Li, "Emerging energy applications of two-dimensional layered transition metal dichalcogenides," *Nano Energy*, vol. 18, pp. 293–305, 2015, doi: 10.1016/j.nanoen.2015.10.023.

[20] X. Zhou *et al.*, "2D Layered Material-Based van der Waals Heterostructures for Optoelectronics," *Adv. Funct. Mater.*, vol. 28, no. 14, pp. 1–28, 2018, doi: 10.1002/adfm.201706587.

[21] X.-G. Gao, X.-K. Li, W. Xin, X.-D. Chen, Z.-B. Liu, and J.-G. Tian, "Fabrication, optical properties, and applications of twisted two-dimensional materials," *Nanophotonics*, vol. 9, no. 7, pp. 1717–1742, 2020, doi: 10.1515/nanoph-2020-0024.

[22] K. S. Novoselov, A. Mishchenko, A. Carvalho, and A. H. Castro Neto, "2D materials and van der Waals heterostructures," *Science (80-.).*, vol. 353, no. 6298, 2016, doi: 10.1126/science.aac9439.

[23] Y. Liu, N. O. Weiss, X. Duan, H.-C. Cheng, Y. Huang, and X. Duan, "Van der Waals heterostructures and devices," *Nat. Rev. Mater.*, vol. 1, no. 9, p. 16042, 2016, doi: 10.1038/natrevmats.2016.42.

[24] J. G. Azadani, C. Yang, S. J. Koester, T. Low, and V. O. Ozc, "Band alignment of two-dimensional semiconductors for designing heterostructures with momentum space matching," vol. 035125, 2016, doi: 10.1103/PhysRevB.94.035125.

[25] Y. Luo *et al.*, "First-Principles Study on Transition-Metal Dichalcogenide/BSe van der Waals Heterostructures: A Promising Water-Splitting Photocatalyst," *J. Phys. Chem. C*, vol. 123, no. 37, pp. 22742–22751, 2019, doi: 10.1021/acs.jpcc.9b05581.

[26] W. Zhang, Q. Wang, Y. Chen, Z. Wang, and A. T. S. Wee, "Van der Waals stacked 2D layered materials for optoelectronics," *2D Mater.*, vol. 3, no. 2, pp. 1–17, 2016, doi: 10.1088/2053-1583/3/2/022001.

[27] Y. Liu, Y. Huang, and X. Duan, "Van der Waals integration before and beyond two-dimensional materials," *Nature*, vol. 567, no. 7748, pp. 323–333, 2019, doi: 10.1038/s41586-019-1013-x.

[28] M. Farmanbar and G. Brocks, "First-principles study of van der Waals interactions and lattice mismatch at MoS2/metal interfaces," *Phys. Rev. B*, vol. 93, no. 8, pp. 1–12, 2016, doi: 10.1103/PhysRevB.93.085304.

[29] S. Santhosh and A. A. Madhavan, "A review on the structure, properties and characterization of 2D Molybdenum Disulfide," *2019 Adv. Sci. Eng. Technol. Int. Conf. ASET 2019*, pp. 1–5, 2019, doi: 10.1109/ICASET.2019.8714360.

[30] M. Serhan *et al.*, *Total iron measurement in human serum with a smartphone*, vol. 2019-Novem. 2019.

[31] L. Ju, M. Bie, J. Shang, X. Tang, and L. Kou, "Janus transition metal dichalcogenides: A superior platform for photocatalytic water splitting," *JPhys Mater.*, vol. 3, no. 2, 2020, doi: 10.1088/2515-7639/ab7c57.

[32] E. Liu *et al.*, "Fabrication of 2D SnS2/g-C3N4 heterojunction with enhanced H2 evolution during photocatalytic water splitting," *J. Colloid Interface Sci.*, vol. 524, no. 229, pp. 313–324, 2018, doi: 10.1016/j.jcis.2018.04.038.

[33] M. A. Rosen and S. Koohi-Fayegh, "The prospects for hydrogen as an energy carrier: an overview of hydrogen energy and hydrogen energy systems," *Energy, Ecol. Environ.*, vol. 1, no. 1, pp. 10–29, 2016, doi: 10.1007/s40974-016-0005-z.

[34] S. Hilliard, "Water splitting photoelectrocatalysis : the conception and construction of a photoelectrocatalytic water splitting cell To cite this version : HAL Id : tel-01358735 Université Pierre et Marie Curie (Paris VI) photoelectrocatalyique pour la photodissocia," 2016.

[35] R. Küngas, " Review—Electrochemical CO 2 Reduction for CO Production: Comparison of Low- and High-Temperature Electrolysis Technologies ," *J. Electrochem. Soc.*, vol. 167, no. 4, p. 044508, 2020, doi: 10.1149/1945-7111/ab7099.

[36] S. a Maier, *Fundamentals and Applications Plasmonics : Fundamentals and Applications*,

vol. 677, no. 1. 2004.

[37] K. Maeda, “Photocatalytic water splitting using semiconductor particles: History and recent developments,” *J. Photochem. Photobiol. C Photochem. Rev.*, vol. 12, no. 4, pp. 237–268, 2011, doi: 10.1016/j.jphotochemrev.2011.07.001.

[38] J. Wang *et al.*, “Intriguing electronic and optical properties of two-dimensional Janus transition metal dichalcogenides,” *Phys. Chem. Chem. Phys.*, vol. 20, no. 27, pp. 18571–18578, 2018, doi: 10.1039/c8cp02612b.

[39] A. W. Welch, L. L. Baranowski, P. Zawadzki, S. Lany, C. A. Wolden, and A. Zakutayev, “CuSbSe2 photovoltaic devices with 3% efficiency,” *Appl. Phys. Express*, vol. 8, no. 8, pp. 1–12, 2015, doi: 10.7567/APEX.8.082301.

[40] J. Wang, M. Zhang, J. Meng, Q. Li, and J. Yang, “Single- and few-layer BiOI as promising photocatalysts for solar water splitting,” *RSC Adv.*, vol. 7, no. 39, pp. 24446–24452, 2017, doi: 10.1039/c7ra01723e.

[41] M. Feng *et al.*, “Interfacial Strain Engineering in Wide-Bandgap GeS Thin Films for Photovoltaics,” *J. Am. Chem. Soc.*, vol. 143, no. 25, pp. 9664–9671, 2021, doi: 10.1021/jacs.1c04734.

[42] M. Javadi, “Theoretical efficiency limit of graphene-semiconductor solar cells,” *Appl. Phys. Lett.*, vol. 117, no. 5, 2020, doi: 10.1063/5.0020080.

[43] X. Roca-Maza and N. Paar, “Nuclear equation of state from ground and collective excited state properties of nuclei,” *Prog. Part. Nucl. Phys.*, vol. 101, pp. 96–176, 2018, doi: 10.1016/j.ppnp.2018.04.001.

[44] L. J. Bartolotti and K. Flurchick, “An Introduction to Density Functional Theory,” *Rev. Comput. Chem.*, vol. 7, pp. 187–216, 2007, doi: 10.1002/9780470125847.ch4.

[45] M. P. Andersson, “Density functional theory with modified dispersion correction for metals applied to molecular adsorption on Pt(111),” *Phys. Chem. Chem. Phys.*, vol. 18, no. 28, pp. 19118–19122, 2016, doi: 10.1039/c6cp03289c.

[46] L. C. Woods and K. A. Redish, “An Introduction to Computational Methods,” *Math. Gaz.*, vol. 48, no. 364, p. 246, 1964, doi: 10.2307/3613592.

[47] J. G. Broida, “Calculus of Variations Calculus of Variations 1 Functional Derivatives,” 2009.

[48] J. L. Bretonnet, “Basics of the density functional theory,” *AIMS Mater. Sci.*, vol. 4, no. 6, pp. 1372–1405, 2017, doi: 10.3934/MATERSCI.2017.6.1372.

[49] M. Freyss and C. De Cadarache, “Chapter 12. Density functional theory,” pp. 225–235, 2015.

[50] J. Paier, R. Hirschl, M. Marsman, and G. Kresse, “The Perdew-Burke-Ernzerhof exchange-correlation functional applied to the G2-1 test set using a plane-wave basis set,” *J. Chem.*

Phys., vol. 122, no. 23, 2005, doi: 10.1063/1.1926272.

[51] H. S. Yu, S. L. Li, and D. G. Truhlar, "Perspective: Kohn-Sham density functional theory descending a staircase," *J. Chem. Phys.*, vol. 145, no. 13, 2016, doi: 10.1063/1.4963168.

[52] A. J. Danner, "An introduction to the empirical pseudopotential method," vol. 1, no. 1, pp. 1–7, 2010, [Online]. Available: http://www.ece.nus.edu.sg/stfpage/eleadj/pseudopotential.htm.

[53] P. Pitriana, T. D. K. Wungu, H. Herman, and R. Hidayat, "The computation parameters optimizations for electronic structure calculation of LiPbl 3 perovskite by the density functional theory method," *IOP Conf. Ser. Mater. Sci. Eng.*, vol. 434, no. 1, 2018, doi: 10.1088/1757-899X/434/1/012026.

[54] J. Kohanoff, "Elements of first-principles electronic structure calculations," no. April, 2010.

[55] P. Giannozzi *et al.*, "QUANTUM ESPRESSO: A modular and open-source software project for quantum simulations of materials," *J. Phys. Condens. Matter*, vol. 21, no. 39, 2009, doi: 10.1088/0953-8984/21/39/395502.

[56] M. J. T. Oliveira *et al.*, "The CECAM electronic structure library and the modular software development paradigm," *J. Chem. Phys.*, vol. 153, no. 2, 2020, doi: 10.1063/5.0012901.

[57] T. V. Ab, S. Package, H. P. C. Wales, H. P. C. Wales, S. S. Bridge, and H. P. C. Wales, "Guide to running VASP Step 1 -Log in,"

[58] H. J. Snaith, "Estimating the maximum attainable efficiency in Dye-sensitized solar cells," *Adv. Funct. Mater.*, vol. 20, no. 1, pp. 13–19, 2010, doi: 10.1002/adfm.200901476.

[59] F. Giustino, M. L. Cohen, and S. G. Louie, "GW method with the self-consistent Sternheimer equation," *Phys. Rev. B - Condens. Matter Mater. Phys.*, vol. 81, no. 11, pp. 1–17, 2010, doi: 10.1103/PhysRevB.81.115105.

[60] W. Shockley and H. J. Queisser, "Detailed balance limit of efficiency of p-n junction solar cells," *J. Appl. Phys.*, vol. 32, no. 3, pp. 510–519, 1961, doi: 10.1063/1.1736034.

[61] S.Piskunov, "The electronic structure of perfect and defective perovskite crystals: Ab initio hybrid functional calculations," no. October, 2003, [Online]. Available: http://d-nb.info/970410433/34.

[62] A. Miralrio, E. Rangel Cortes, and M. Castro, "Electronic properties and enhanced reactivity of MoS 2 monolayers with substitutional gold atoms embedded into sulfur vacancies," *Appl. Surf. Sci.*, vol. 455, pp. 758–770, 2018, doi: 10.1016/j.apsusc.2018.05.220.

[63] F. Li, W. Wei, P. Zhao, B. Huang, and Y. Dai, "Electronic and Optical Properties of Pristine and Vertical and Lateral Heterostructures of Janus MoSSe and WSSe," *J. Phys. Chem. Lett.*, vol. 8, no. 23, pp. 5959–5965, 2017, doi: 10.1021/acs.jpclett.7b02841.

[64] S. Ahmad, I. Ahmad, N. Van, and B. Amin, "Intriguing electronic structure and

photocatalytic performance of blueP-SMSe and blueP-SeMS (M = Mo, W) van der Waals heterostructures," *RSC Adv.*, vol. 10, no. 62, pp. 38114–38119, 2020, doi: 10.1039/d0ra07000a.

[65] M. Yagmurcukardes, C. Sevik, and F. M. Peeters, "Electronic, vibrational, elastic, and piezoelectric properties of monolayer Janus MoSTe phases: A first-principles study," *Phys. Rev. B*, vol. 100, no. 4, pp. 1–8, 2019, doi: 10.1103/PhysRevB.100.045415.

[66] X. Yang, D. Singh, Z. Xu, Z. Wang, and R. Ahuja, "An emerging Janus MoSeTe material for potential applications in optoelectronic devices," *J. Mater. Chem. C*, vol. 7, no. 39, pp. 12312–12320, 2019, doi: 10.1039/c9tc03936h.

[67] H. G. Abbas, T. Debela, R. Hahn, H. Seok, and N. Carolina, "Multiferroicity of Non-Janus MXY (X = Se / S , Y = Te / Se) Monolayers with Giant In-Plane Ferroelectricity of Nano and Advanced Materials , College of Engineering , Jeonju University , monolayers in the 1H phase . Lattice parameters are the same for al," pp. 1–5.

[68] A. Patel, D. Singh, Y. Sonvane, P. B. Thakor, and R. Ahuja, "High Thermoelectric Performance in Two-Dimensional Janus Monolayer Material WS-X (X = Se and Te)," *ACS Appl. Mater. Interfaces*, vol. 12, no. 41, pp. 46212–46219, 2020, doi: 10.1021/acsami.0c13960.

[69] T. V. Vu *et al.*, "Graphene/WSeTe van der Waals heterostructure: Controllable electronic properties and Schottky barrier via interlayer coupling and electric field," *Appl. Surf. Sci.*, vol. 507, no. December 2019, p. 145036, 2020, doi: 10.1016/j.apsusc.2019.145036.

[70] I. A. Rahman and A. Purqon, "First Principles Study of Molybdenum Disulfide Electronic Structure," *J. Phys. Conf. Ser.*, vol. 877, no. 1, 2017, doi: 10.1088/1742-6596/877/1/012026.

[71] S. Deng, L. Li, and P. Rees, "Graphene/MoXY Heterostructures Adjusted by Interlayer Distance, External Electric Field, and Strain for Tunable Devices," *ACS Appl. Nano Mater.*, vol. 2, no. 6, pp. 3977–3988, 2019, doi: 10.1021/acsanm.9b00871.

[72] L. Ju, M. Bie, X. Tang, J. Shang, and L. Kou, "Janus WSSe Monolayer: An Excellent Photocatalyst for Overall Water Splitting," *ACS Appl. Mater. Interfaces*, vol. 12, no. 26, pp. 29335–29343, 2020, doi: 10.1021/acsami.0c06149.